A Mesoscale Model for the Simulation of Turbulence, Clouds and Flow over Mountains: Formulation and Validation Examples

Ulrich Schumann, Thomas Hauf, Hartmut Höller, Helmut Schmidt and Hans Volkert
DFVLR, Institut für Physik der Atmosphäre, D-8031 Oberpfaffenhofen

(Manuscript received 10.02.1987, in revised form 26.05.1987)

Abstract:
A three-dimensional numerical model (MESOSCOP) is formulated for the simulation of mesoscale (and microscale) atmospheric processes. Presently, three versions are used to study clouds and precipitation processes above flat terrain, airflow over mountains and turbulent boundary layers. The model's equations describe non-hydrostatic flows for an incompressible or a compressible fluid. Entropy is used as prognostic variable for a general thermodynamic treatment of dry and moist air. Turbulent fluxes are parametrized by closures of first or second order. The cloud microphysics section takes into account five classes of liquid and ice phase constituents. Various numerical and technical features allow to operate with large numbers of grid cells and also permit versatile combinations of boundary conditions.

Five validation examples demonstrate the scope of the model: a rising thermal, gravity waves over mountains, retardation of an idealized cold front at a mountain ridge, convective boundary layer and precipitating cumulus convection. The model is quantitatively validated by comparisons to reference solutions, which are exact or numerical or stem from dimensional analysis. Furthermore, recalculations are presented for a laboratory experiment and for an atmospheric case in which detailed cloud physical field observations are available.

Zusammenfassung: Ein Mesoskalen-Modell zur Berechnung von Turbulenz, Wolken und Gebirgsüberströmung: Formulierung und Beispiele zur Modellüberprüfung
Ein dreidimensionales numerisches Modell (MESOSCOP) wird beschrieben, mit dem mesoskalige (und mikroskalige) atmosphärische Prozesse simuliert werden können. Es existiert gegenwärtig in drei Versionen und erlaubt, Wolken und Niederschlagsbildung über ebenem Gelände, Gebirgsüberströmungen und turbulente Grenzschichten zu untersuchen. Die Modellgleichungen beschreiben nicht-hydrostatische Strömungen mit wahlweise inkompressiblem oder kompressiblem Fluid. Entropie wird als prognostische Variable zur einheitlichen Behandlung der Thermodynamik in trockener und feuchter Luft benutzt. Für die Parametrisierung turbulenter Flüsse stehen Schließungsansätze erster oder zweiter Ordnung bereit. Das Wolken-Mikrophysikmodell enthält Ansätze für fünf Klassen flüssiger oder eisförmiger Bestandteile. Numerische und programmtechnische Komponenten ermöglichen große Gitterpunktzahlen und vielseitige Kombinationen von Randbedingungen.

Die Anwendungsbreite des Modells wird anhand von fünf Beispielen demonstriert: aufsteigende Warmluftblase, Schwerewellen über einem Berg, Verzögerung einer idealisierten Kaltfront an einem Berg, konvektive Grenzschicht und Cumulus-Konvektion mit Niederschlagsbildung. Das Modell wird quantitativ überprüft durch Vergleiche mit dimensionanalytischen, exakten und numerischen Referenzlösungen. Weiterhin werden Nachrechnungen eines Laborexperiments und eines atmosphärischen Falles vorgestellt, für den detaillierte Beobachtungsdaten zur Wolkenphysik vorliegen.

Résumé: Un modèle à mésoéchelle pour la simulation de la turbulence, des nuages et de l'écoulement en montagne: formulation et exemples de validation

On formule un modèle numérique (MESOSCOP) à trois dimensions pour la simulation de processus atmosphériques de mésoéchelle (et de microéchelle). Trois versions sont actuellement utilisées pour étudier les nuages et les précipitations en terrain plat, l'écoulement de l'air au-dessus de montagnes et les couches limites turbulentes. Les équations du modèle s'appliquent à des écoulements non hydrostatiques d'un fluide compressible ou incompressible. Afin de traiter de manière générale l'air sec et l'air humide, on utilise l'entropie comme variable pronostique. Les flux turbulents sont paramétrisés par fermetures de premier et second ordre. La microphysique des nuages prend en compte cinq classes de constituants en phase liquide ou sous forme de glace. Divers artifices numériques et techniques permettent de travailler avec un grand nombre de cellules de grille ainsi que l'usage de divers types de conditions aux limites.

Cinq exemples de validation illustrent les objectifs du modèle: une thermique ascendante, des ondes de gravité au-dessus de montagnes, le ralentissement par une montagne d'un front froid idéalisé, une couche limite convective et la convection de cumulus précipitants. Le modèle est validé quantitativement par comparaison avec des solutions de référence exactes ou numériques ou résultant d'analyse dimensionnelle. De plus, on présente des calculs complémentaires relatifs à une expérience en laboratoire et à un cas atmosphérique pour lequel des observations détaillées de la physique des nuages sont disponibles.

1 Introduction

On the mesoscale the atmosphere exhibits a variety of interesting flow phenomena. In defining this intermediate range in length scales between the macroscale of cyclones and microscale of pure turbulence we follow the approach by ATKINSON (1981, 1984): typical frequencies of mesoscale processes are larger than the Brunt-Väisälä frequency N of free vertical oscillations in the stratified atmosphere and smaller than the inertial frequency due to the earth's rotation f; the corresponding length scales depend upon the flow velocity and typically range from 1 to 100 kilometres. Examples of interesting phenomena are, e.g. severe local storms, thermals in boundary layers, mountain and lee waves, and the orographic modification of fronts. This short list illustrates the wide band of scales which interact within the mesoscale.

As described by PIELKE (1984) numerical models have proven to be powerful tools for enlarging the basic knowledge of the dominant mesoscale processes and for applied studies. Any model is based on a set of approximations, which stem from choices in at least four categories: the set of equations, the prescription of boundary conditions, the kind of parametrizations and the numerical schemes. At mesoscales typical simplifications of the equations concern the treatment of vertical accelerations (hydrostatic or non-hydrostatic) and the continuity equation (non-divergent: $\operatorname{div} \vec{v} = 0$; anelastic: $\operatorname{div} \rho\vec{v} = 0$; full continuity). Within the equations of motion, density can be treated variable everywhere or only in the buoyancy term (Boussinesq approximation). Such approximations simplify the construction of the respective model and may improve the numerical efficiency considerably.

To characterize the state of the art we list some examples for three-dimensional mesoscale models: MAHRER and PIELKE (1977) and NICKERSON et al. (1986) use the hydrostatic and non-divergent approximations. The former model is applied *inter alia* to the simulation of mountain-valley winds and airflow over mountains, while the latter contains a microphysical parametrization for clouds and rain and has been applied to flows over the Vosges and Black forest mountains. CLARK (1977 [dry version], 1979 [with cloud physical parametrizations]) and GROSS (1985; program FITNAH) published anelastic models. The first one is applied, for instance, to airflows over mountains and to cumulus clouds, the other to circulations in valleys and the propagation of isolated sand dunes. TRIPOLI and COTTON (1982) provide an example for a full continuity model; it uses time step splitting to avoid noise amplification by sound waves and incorporates detailed microphysical parametrizations.

Moreover, several alternatives exist for the proper selection of the thermodynamic variable and the related prognostic equation. For simulating dry air, potential temperature is the common choice because it remains constant for adiabatic and reversible processes. For moist and cloudy air several generalized potential temperature concepts have been proposed (e.g. ice-liquid water potential temperature by TRIPOLI and COTTON, 1981). One advantage of such conservative variables is that they are smoothly varying variables along streamlines even if clouds are forming and thus less susceptible to numerical approximation errors. These temperature proposals are approximations to a general entropy-temperature; hence the entropy balance equation offers the most general concept (HAUF and HÖLLER, 1987).

Returning to the atmospheric mesoscale as a whole, we see from the studies by OGURA and PHILIPPS (1962) and WIPPERMANN (1981) that the mentioned approximations are not valid for the entire range of length scales and for all processes of interest. The efficiency gained by the use of approximations may be overcompensated by the limitations of the model's accuracy. Moreover, the validity of the approximations used is often difficult to examine, if non-linear interactions between scales dominate. It seems, therefore, preferable to have a model, which provides the possibility to select from several approximative levels. This opens the field to study flow/scale interactions and to check in concrete situations the validity of approximations, which normally are based on scale analysis arguments.

The modelling effort reported here was started with the aim to build a rather general mesoscale model, which allows to invoke more stringent approximations. The resultant code, termed MESOSCOP (acronym for mesoscale flow and cloud model Oberpfaffenhofen), can deal with non-hydrostatic, anelastic as well as with fully compressible flows, with variable or Boussinesq approximated density. The prognostic equations are formulated in budget form and entropy is used as thermodynamic variable. A terrain following coordinate transformation accounts for an irregular lower boundary in applications with orography. Parametrizations for liquid and ice phase processes and a first or second order model represent cloud physics and turbulence, respectively. The numerical algorithm uses centred differences and a combination of the Adams-Bashforth and the Smolarkiewicz integration schemes. All these model design and technical aspects are described in Section 2.

Section 3 is devoted to model validation. Furthermore, it demonstrates the feasibility of a mesoscale model with a wide range of application. This is achieved by simulating in sequence flows for which either non-linear analytical solutions are known, or which were measured in the laboratory or which were observed in detail in a field experiment. This climax seems a necessary step during the development of a complex mesoscale model (see PIELKE, 1984, p. 421), yet we are not aware that a similar study has been published for any of the three-dimensional models mentioned. The range of flows, which can be studied by applying MESOSCOP, is demonstrated by the fact that the validation examples comprise microscale flows (self similarity of a rising thermal, large eddy simulation of a turbulent laboratory flow), a non-hydrostatic mesoscale flow (development of a precipitating cumulus) and hydrostatic mesoscale flows (mountain waves and propagation of an idealized cold front).

2 Formulation of the Numerical Model

Presently, three versions of MESOSCOP exist, as the development from a general concept was started simultaneously for three mesoscale processes. Version A in Cartesian coordinates and with cloud microphysical parametrizations treats convective clouds, version B in terrain following coordinates deals with airflow over complex terrain and version C in Cartesian coordinates and with advanced turbulence parametrizations is tailored for turbulent boundary layer studies. Common to all versions are the basic model equations, the spatial and time discretizations, an elliptic equation for pressure, specification of boundary conditions, the data flow structure and a modular programming concept. All these aspects constitute the subject of this section. However, the coordinate transformation, the parametrization of turbulence and the cloud microphysics model are described only briefly; they are documented elsewhere.

2.1 Basic Model Equations

MESOSCOP is based on the conservation laws for density ρ, velocity $\vec{v}$ or volume specific momentum $\rho\vec{v}$, and several mass specific scalars ψ_k, $k = 1, ..., K$. The number K and the meaning of the scalars depend on the specific applications. The conservation laws are expressed by budget equations (see Appendix A for a complete list of symbols):

$$\frac{\partial \rho}{\partial t} + \operatorname{div}(\rho\vec{v}) = 0, \tag{1}$$

$$\frac{\partial \rho\vec{v}}{\partial t} + \operatorname{div}(\rho\vec{v}\vec{v}) + 2\vec{\Omega} \times (\rho\vec{v}) + \operatorname{div}(F) = -\vec{\operatorname{grad}}(p) - \rho\,\vec{g}, \tag{2}$$

$$\frac{\partial \rho\psi_k}{\partial t} + \operatorname{div}(\rho\vec{v}\,\psi_k) + \operatorname{div}(\vec{f}_k) = \rho\, q_k; \qquad k = 1, ..., K. \tag{3}$$

Equation (1) is the continuity equation for variable density. Equation (2) describes the nonhydrostatic momentum balance and includes Coriolis forces due to earth's rotation $\vec{\Omega}$, friction by diffusive momentum fluxes F, pressure p, and gravity $\vec{g}$. Equation (3) expresses the budget of a scalar ψ_k with non-advective fluxes $\vec{f}_k$, and mass specific sources q_k.

The present 'conservative' form of the budget is chosen, because it aids in ensuring that sums of local contributions to time derivatives from all discrete grid volumes are equivalent to integrals for the budgets in the original continuum formulation so that integral conservation of mass, momentum and volume specific concentrations $\rho\psi_k$ is guaranteed at least up to errors induced by approximations of time derivatives (CLARK, 1977) regardless of how accurate the local approximations are. Moreover, the sum of the budget equations for mass specific concentrations of air components is equivalent to Equation (1) under the constraint that the summed fluxes and sources vanish.

In order to reduce numerical approximation errors and to provide a reference state for linearizations, the pressure gradient and buoyancy terms of the momentum equation deal with deviations p', ρ' from a hydrostatic reference state

$$\vec{\operatorname{grad}}\,[\bar{p}(z)] = -\bar{\rho}(z)\,\vec{g}; \qquad p' = p - \bar{p}(z); \qquad \rho' = \rho - \bar{\rho}(z). \tag{4}$$

Further, it is convenient (e.g. because of simplified boundary conditions) to include a synoptic part p_G of the pressure p as a function of a prescribed geostrophic momentum $(\rho\vec{v})_G$ within the Coriolis accelerations of Equation (2),

$$\vec{\operatorname{grad}}\,(p_G) = -2\,\vec{\Omega} \times (\rho\vec{v})_G. \tag{5}$$

To complete the system, equations of state

$$\rho = \rho\,(p, \psi_k), \qquad T = T\,(p, \psi_k), \tag{6}$$

have to be provided. Absolute temperature T is only necessary in the parametrizations for fluxes and sources, e.g. for cloud microphysics. (In the applications considered so far, the influence of geostrophic variations of pressure is neglected with respect to the equations of state, partly because its effect is small on mesoscales, partly for technical reasons.)

For most applications a linearized equation of state

$$\rho = \bar{\rho} + A_p(p - \bar{p}) + \sum_{k=1}^{K} A_k\,(\psi_k - \bar{\psi}_k), \qquad A_p = \frac{\partial \rho}{\partial p}, \qquad A_k = \frac{\partial \rho}{\partial \psi_k}, \tag{7}$$

is used; the coefficients A_p, A_k are computed from the hydrostatic reference state, $\bar{p}$, $\bar{\psi}_k$, $\bar{\rho} = \rho(\bar{p}, \bar{\psi}_k)$. A_p is the inverse of the squared velocity of sound and vanishes for incompressible fluids. Details for cloudy air are specified in Section 2.2.

Equations (1) to (3) are formally defined for laminar flows but can be applied to turbulent flows as well where ρ, $\rho\vec{v}$, and ψ_k denote suitable (ensemble or volume averaged) mean values. Only the meaning of the fluxes has to be extended to include turbulent contributions $\overline{(\rho\vec{v})'\vec{v}'}$ and $\overline{(\rho\vec{v})'\psi_k'}$, where the primes refer to local deviations from the respective mean values. We distinguish between turbulent (in special cases purely diffusive) and precipitational (gravitational) parts of fluxes, i.e.

$$F = F^t + F^p, \qquad \vec{f}_k = \vec{f}^{\,t}_k + \vec{f}^{\,p}_k. \tag{8}$$

In the applications, the second part is neglected except for precipitating clouds as explained in Section 2.7. Turbulent fluxes are computed as described in Section 2.6.

Although the method allows for variable density, the Boussinesq approximation is used for cases where we compare our computational results with corresponding theories or where density fluctuations are very small as in simulations of water flows. In this approximation, ρ equals $\bar{\rho}(z)$ everywhere except in the buoyancy term. As a consequence the anelastic approximation $\operatorname{div}(\bar{\rho}\vec{v}) = 0$ is invoked (as $\partial\bar{\rho}/\partial t = 0$).

2.2 Thermodynamics of Cloudy Air

For cloudy air, thermodynamics are expressed in terms of entropy s, and mass specific concentrations m^i, $i = 1, 2, 3$, for vapour, liquid and ice water, respectively. These variables are associated with prognostic fields $\psi_1 = s$, $\psi_2 = m^1$ and with concentrations of cloud particles as described in Section 2.7. In the absence of further air components, the concentration of dry air is $m^0 = 1 - m^1 - m^2 - m^3$, so that no separate budget equation is necessary for m^0. The precise definitions of sources and fluxes in the budget equations (Equation 3) for entropy and water phase concentrations are given in DEGROOT and MAZUR (1969, pp. 17 and 28).

The equations of state for cloudy air read:

$$\rho = \frac{p}{R_m T}, \qquad R_m = R_0 m^0 + R_1 m^1, \tag{9}$$

$$s = \sum_{i=0}^{3} s_i m^i, \quad s_i = c_p^i \ln\frac{T}{T_*} - R_i \ln\frac{p^i}{p_*} + s_i^*, \quad p^i = m^i p \frac{R_i}{R_m}, \quad i = 0, 1, 2, 3, \tag{10}$$

where R_i ($R_2 \equiv R_3 \equiv 0$), c_p^i, s_i^*, p_* and T_* denote gas constants, constant specific heats and entropy reference values for the concentrations i, as well as reference values for pressure and temperature, respectively. The reference values of entropy are given in HAUF and WEIDNER (1986).

Equation (10) can be inverted to evaluate the temperature:

$$T = T_* \exp\left[\frac{1}{c_p}\left(s - s^* + R_0 m^0 \ln\frac{p^0}{p_*} + R_1 m^1 \ln\frac{p^1}{p_*}\right)\right],$$

$$c_p = \sum_{i=0}^{3} m^i c_p^i, \qquad s^* = \sum_{i=0}^{3} m^i s_i^*. \tag{11}$$

The derivatives required for a linearized equation of state (Equation 7) can be given explicitly:

$$\frac{\partial \rho}{\partial p} = \frac{\rho(c_p - R_m)}{c_p\, p}, \qquad \frac{\partial \rho}{\partial s} = -\frac{\rho}{c_p},$$

$$\frac{\partial \rho}{\partial m^1} = \rho\left(\frac{s_1 - s_0}{c_p} + \frac{R_0 - R_1}{R_m}\right), \qquad \frac{\partial \rho}{\partial m^i} = \rho\left(\frac{s_i - s_0}{c_p} + \frac{R_0}{R_m}\right), \quad i = 2, 3. \tag{12}$$

Entropy in contrast to enthalpy or internal energy has the advantage that the entropy source vanishes for reversible processes. Thus, the coupling between the equation for entropy and all other equations is looser than it would be for other thermodynamical variables. This decoupling is important with respect to pressure in the numerical integration scheme since pressure is to be treated implicitly. Moreover, since the sources are rather small even with irreversible processes, entropy is a smooth function along streamlines. Entropy is an extensive quantity and hence ρs satisfies a budget equation. In contrast, absolute temperature T and potential temperature θ, e.g. defined for dry air by

$$\theta = T\left(\frac{p}{p^*}\right)^{-R_0/c_p^0} \tag{13}$$

are intensive quantities so that ρT or $\rho\theta$ generally do not satisfy a budget equation. However, potential temperature is conserved for reversible processes in a perfect gas (with c_p^0 = const). Therefore, we use potential temperature as an alternative to entropy for dry air under such assumptions. In this case $\partial\rho/\partial p$ is given by Equation (12) and $\partial\rho/\partial\theta = -\rho/\theta$.

2.3 Discretization and Pressure Equation

For numerical integration, we use a finite difference method. The computational domain is discretized by a staggered grid. All scalars are defined at cell centres while vector components are located in the middle of the corresponding interfaces between grid cells (see Figure 1). For time, we distinguish discrete time levels t^n with the time step $\Delta t = t^{n+1} - t^n$ being constant for at least a few integration steps. As subsequently explained, a semi-implicit time integration scheme is used, which casts Equations (1) to (5) into

$$\frac{(\rho^{n+1} - \rho^n)}{\Delta t} + \mathrm{div}(\rho\vec{v})^{n+1} = 0, \tag{14}$$

$$(\rho\vec{v})^{n+1} = (\rho\vec{v})^{\sim} - \Delta t\, \vec{\mathrm{grad}}\,(\Delta p), \tag{15}$$

$$(\rho\psi_k)^{n+1} = (\rho\psi_k)^n - \Delta t\,[\mathrm{div}(\rho\vec{v}\,\psi_k) + \mathrm{div}(\vec{f}_k)]^n + \Delta t\,\rho\, q_k, \tag{16}$$

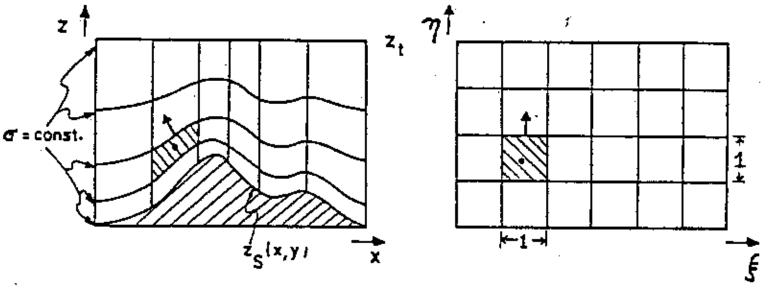

Figure 1
Typical cross-section through domain. Left: physical space with orography; right: transformed computational space consisting of unit cubes.

with the abbreviations

$$(\rho\vec{v})^{\sim} = (\rho\vec{v})^n - \Delta t\,[\gamma_0\,\vec{b}^n + \gamma_1\,\vec{b}^{n-1} + \vec{\mathrm{grad}}\,(p')^n + (\rho^{\sim} - \bar{\rho})\,\vec{g}], \tag{17}$$

$$\rho^{\sim} = \rho(p^n, \psi_k^{n+1}), \quad \Delta p = (p')^{n+1} - (p')^n, \tag{18}$$

$$\vec{b} = \mathrm{div}\,(\rho\vec{v}\vec{v}) + 2\,\vec{\Omega} \times [\rho\vec{v} - (\rho\vec{v})_G] + \mathrm{div}(F) \tag{19}$$

and the density specification

$$\rho^{n+1} = \begin{cases} \rho^n & \text{for Boussinesq calculation,} \\ \rho^{\sim} + A_p\,\Delta p & \text{otherwise.} \end{cases} \tag{20}$$

Initially and after changes of Δt, one Euler step is applied ($\gamma_0 = 1, \gamma_1 = 0$); otherwise the Adams-Bashforth scheme is used ($\gamma_0 = 1.5, \gamma_1 = -0.5$).

All advection terms are treated explicitly because we assume that the resultant time step constraint has to be satisfied anyway to achieve sufficient accuracy. For the advection of scalars we choose the second-order upwind scheme by SMOLARKIEWICZ (1984) because it guarantees that positive scalars stay positive at the expense of only small numerical diffusion errors. Otherwise, spatial differentials are approximated by second-order accurate central differences in a form which conserves kinetic energy both for constant and variable density (SCHUMANN, 1984). The Adams-Bashforth scheme is preferred to the leapfrog scheme, because it does not exhibit spurious oscillations in time and it is second order accurate with respect to diffusion. Its instability (amplification factor of order $1 + O(\Delta t^4)$) for inviscid flows is so weak that it does not form a restriction in practice. The combination of the Smolarkiewicz-scheme for scalars, in which advective fluxes are based on the momentum fluxes for time t^n, with the integration scheme for momentum makes it necessary to evaluate the density $\rho^{\sim}$ from the most recent scalar fields, see Equation (18). The source term q_k in Equation (16) is treated explicitly in most situations; only fast processes like cloud condensation or dissipation of turbulent kinetic energy need implicit treatment in order to avoid time step restrictions. The time integration algorithm and the explicit or implicit treatment of source terms are given in Appendix B.

The integration scheme is approximately of second order accuracy. It is numerically stable if

$$\Delta t < \min\left[\frac{\Delta}{2U}, \frac{2}{N}, \frac{\Delta^2}{2K_M}\right], \tag{21}$$

where Δ, U, N, and K_M denote the typical grid spacing, the maximum advection velocity, the Brunt-Väisälä frequency and the maximum relevant diffusivity.

The implicit approximation to mass continuity, pressure and density (Equations 14, 15, 18) filters fast propagating sound waves and hence avoids more stringent constraints on the time step (HARLOW and AMSDEN, 1971). However, it requires the implicit determination of pressure, so that the momentum resulting from Equation (15) satisfies Equation (14). Substitution of Equations (15) and (20) into Equation (14) yields an elliptic equation of Helmholtz type for the pressure increment

$$\mathrm{div}\,\vec{\mathrm{grad}}\,(\Delta p) - \frac{A_p}{\Delta t^2}\,\Delta p = \frac{1}{\Delta t}\,\mathrm{div}(\rho\vec{v})^{\sim} + \frac{1}{\Delta t^2}(\rho^{\sim} - \rho^n) \tag{22}$$

which reduces to a Poisson equation for incompressible flow ($A_p = \partial\rho/\partial p = 0$). Additionally, the last term vanishes in the Boussinesq variant (see Appendix B).

In Cartesian grids with constant horizontal grid spacings and $A_p = A_p(z)$ this equation is solved directly via eigenfunction decomposition and fast Fourier transforms in the horizontal directions together with Gaussian elimination in the vertical direction (WILHELMSON and ERICKSEN, 1977). Vectorized algorithms have been developed which allow the application of fast Fourier transforms not only for periodic but also for all other boundary conditions (SCHUMANN and SWEET, 1987). For cases with variable coefficients (due to variable A_p or to variable grid spacings in the horizontal directions or to terrain following coordinates, see below) the direct methods are used to solve the elliptic equation by a block iteration (SCHUMANN and VOLKERT, 1984).

2.4 Boundary Conditions

A common problem to limited area modelling lies in the adequate specification of boundary conditions. Subsequently, we explain the treatment of boundary conditions at the six surfaces of the computational domain. MESOSCOP provides a set of boundary types from which to choose at each surface.

PERI	periodic (not implemented for bottom and top boundary).
CLOS	prescribed inflow with prescribed diffusive fluxes; this simulates a closed wall, if both inflow and fluxes vanish.
FLUX	prescribed inflow with computed diffusive fluxes; fluxes are taken from the gradients at the boundary.
OUTF	free outflow with zero gradients; the normal derivative of all prognostic variables is prescribed. At the top boundary a BKD condition (see below) is used for the pressure.
RADI	radiating; the normal derivative of the normal velocity vanishes. All other prognostic fields satisfy a radiation condition of Sommerfeld-type (not implemented for bottom and top boundary).

These types determine the mathematical boundary conditions for all variables as exemplified in Table 1 for the western side of the domain.

■ **Table 1** Relation between non-periodic boundary types and mathematical boundary conditions for various classes of variables. Boundary types are explained in the text. The boundary condition algorithms are exemplified for the western boundary with F(1), F(2) as boundary value and adjacent interior value, respectively:

DIR – Dirichlet [$F(1) = -s \cdot F(2) + (1 + s) \cdot BV$; s: stagger switch, $s = 1$ if variable is staggered relative to boundary, $s = 0$ otherwise; BV: specified boundary value];

NEU – Neumann [$F(1) = F(2) - BV/\Delta x$; BV: specified boundary value; Δx: mesh size at boundary];

NERA – Neumann radiating [$F(1) = \tilde{F}(1) \cdot (1 - C) + F(2) \cdot C$; $C = -U\ \Delta x/\Delta t$ if $0 < C$; $C = 0$ otherwise; U: normal velocity at boundary; Δx: mesh size at boundary; Δt: time step; $\tilde{F}(1)$: boundary value, predicted as in the interior but with vanishing normal gradients];

------ – boundary value unchanged from specification within routines for interior domain.

var. class \ phys. boundary type	CLOS	FLUX	OUTF	RADI
normal velocity component	DIR	DIR	----	----
tangential velocity components	NEU	DIR	NEU	NERA
normal comp. of normal flux	----	----	NEU	NEU
normal comp. of other fluxes	DIR	----	----	----
density, velocity deformation	NEU	NEU	NEU	NEU
other scalars	NEU	DIR	NEU	NERA

The boundary conditions for pressure are kinematically related to those for the independent fields. Types CLOS and FLUX require prescription of the normal velocity, e.g. $\rho u = BV$ at the western surface (BV: boundary value). This boundary condition is implemented at plane surfaces by setting $\rho u^{\sim} = BV$ after the explicit part of the integration step, see Equation (17). As a consequence, $\rho u^{n+1} = BV$ results from Equation (15) in conjunction with a homogeneous Neumann boundary condition for pressure ($\partial(\Delta p)/\partial x = 0$; the curved lower boundary in terrain following coordinates requires special treatment, see below). For types OUTF and RADI at lateral boundaries, we set $\partial(\rho u^{\sim})/\partial x = 0$ and obtain $\partial(\rho u^{n+1})/\partial x = 0$ from Equation (15), if $\partial^2(\Delta p)/\partial x^2 = 0$. Therefore, the pressure equation degenerates to a two-dimensional problem at such open surfaces. If open surfaces intersect, corresponding one-dimensional problems have to be solved at the corner lines. The solution of these lower dimensional equations yields Dirichlet-type boundary values for the respective interior. For type PERI, periodic boundary conditions are to be applied for the pressure as for all other fields. If Neumann or periodic boundary conditions apply for the pressure at all surfaces, and if the flow is incompressible ($A_p = 0$) the Poisson equation becomes singular. In such cases we require that the horizontal mean of p' vanishes at the top of the computational domain.

The staggered grid has to be defined consistent with the boundary conditions. The grid is defined such that boundaries coincide with grid cell interfaces for boundary types CLOS and FLUX, because this makes prescription of normal velocities unique. For types OUTF and RADI lateral boundaries are defined at grid cell centres because only then standard (non-staggered) Dirichlet boundary conditions result for the pressure in the interior. At the top of the model, cell interfaces make up the boundary, as this has been found necessary in terrain following coordinates.

The specification of OUTF at the top boundary implies special treatment for the boundary values of pressure (following BOUGEAULT, 1983; KLEMP and DURRAN, 1983). Essential for this 'BKD condition' is the proportionality in Fourier space (symbolized by ^) between pressure and the vertical momentum component

$$\hat{p}' = \begin{cases} \frac{N}{|k|}\,(\widehat{\rho w}) & \text{if} \quad N > 0,\ |k| > 0 \\ 0 & \text{otherwise} \end{cases} \tag{23}$$

where $|k|$ and N denote the effective wave number and the Brunt-Väisälä frequency. The eigenfunctions of the discrete Fourier transformation are chosen to be consistent with the specified lateral boundary conditions. Equation (23) is implemented implicitly as proposed by Bougeault [$(\rho w)^{n+1}$ is used rather than $(\rho w)^{\sim}$]. It should be noted that the BKD condition is strictly valid only for hydrostatic, non-rotating (no Coriolis forces) systems.

2.5 Terrain Following Coordinate Transformation

There are several ways of representing the irregular lower boundary in meteorological models (see PIELKE, 1984, chapter 6.2, for a review). In version B of MESOSCOP we follow CLARK (1977) and use the terrain following coordinate

$$\sigma(x, y, z) = z_t \frac{z - z_s(x, y)}{z_t - z_s(x, y)} \tag{24}$$

to resolve the flow domain between the height $z_s(x, y)$ of the irregular, but steadily variying terrain and the height z_t of the model top. Additionally, transformations $\xi(x)$, $\chi(y)$ and $\eta(\sigma)$ allow for variable resolution. These transformations are defined in the discrete system by input tables such that the grid spacing in the transformed coordinates equals unity (see Figure 1). Within the transformed coordinates we apply CLARK's semi-Cartesian approach, i.e. formulate the basic equations for all scalars and for the Cartesian momentum components with derivatives computed from the transformed coordinates. This has the advantage that no additional accelerations arise from changes in the direction of unit vectors. The velocity components normal to coordinate surfaces (u^1, u^2, u^3) are related to the Cartesian components ($u_1 \equiv u, u_2 \equiv v, u_3 \equiv w$) by metric coefficients G^{ij},

$$u^i = G^{ij} u_j \quad \text{with} \quad G^{ij} = \frac{\partial \bar{x}_i}{\partial x_j}, \tag{25}$$

where $\bar{x}_i = (\zeta, \chi, \eta)$, $x_i = (x, y, z)$, $i = 1, 2, 3$, and summation is implied for repeated indices. The coefficients G^{ij} are non-zero only for $ij = (11, 22, 31, 32, 33)$. The Jacobian V of the transformation, and the general definitions of the divergence operator and of the Cartesian gradient operator components

$$\begin{aligned} V &= [G^{11} \cdot G^{22} \cdot G^{33}]^{-1}, \\ V \operatorname{div}(\rho \vec{v} \psi) &= \frac{\partial a^1 \psi}{\partial \xi} + \frac{\partial a^2 \psi}{\partial \chi} + \frac{\partial a^3 \psi}{\partial \eta} \quad \text{with} \quad a^i = \rho V G^{ij} u_j, \quad i = 1, 2, 3, \\ V \,\vec{\text{grad}}(\psi) &= \left(\frac{\partial V G^{11} \psi}{\partial \xi} + \frac{\partial V G^{31} \psi}{\partial \eta} \,\middle|\, \frac{\partial V G^{22} \psi}{\partial \chi} + \frac{\partial V G^{32} \psi}{\partial \eta} \,\middle|\, \frac{\partial V G^{33} \psi}{\partial \eta} \right) \end{aligned} \tag{26}$$

are used to obtain the terrain following version of the basic model equations. Here ψ stands for 1, $\bar{v}$ or ψ_k. In contrast to GROSS (1985), but similar to CLARK (1977), both operators contain only pure differential quotients rather than products of metric terms and differential quotients. As a consequence, conservation of mass and momentum is guaranteed not only for small, but also for arbitrary mesh sizes within the discrete model equations.

The present approach is limited to mountains with slopes of less than about 45° (steeper orography needs more general grid transformations), but a dimensional separation for the metric coefficients, i.e. $G^{ij}(x, y, z) = L^{ij}(z) \cdot H^{ij}(x, y)$, drastically reduces the storage requirements. Details including the discrete representation of Jacobian and metric coefficients are described in SCHUMANN and VOLKERT (1984).

The lower boundary condition at $\eta = 0$ implies $a^3 = 0$ for types CLOS and FLUX. For the pressure an inhomogeneous Neumann condition results from the upward component of Equation (15), as a^3 is a linear combination of the ρu_j and none of the $\rho u_i^{\sim}$ can be specified in such a way as to make the pressure boundary condition homogeneous. The elliptic pressure equation (Equation 22) in terrain following coordinates yields a 25-point operator with variable coefficients. It is solved iteratively by inverting the pressure equation for constant (mean) surface height for the respective residuum (SCHUMANN and VOLKERT, 1984). Both these equations resemble each other more closely if they are formulated in terms of $V \Delta p$ instead of Δp, with a faster convergence as consequence. With regards to the evaluation of $\operatorname{div}(\rho \vec{v} \psi_k)$ by the Smolarkiewicz-scheme, it is essential for the sake of accuracy to use $\rho \vec{v}$ when applying curvilinear coordinates (and also Cartesian grids with variable density) to advect ψ_k rather than using $\vec{v}$ to advect $\rho \psi_k$.

2.6 Parametrization of Turbulence

The choice of how to parametrize turbulent fluxes depends on the relative importance of such fluxes in comparison to other transports. For example, one-dimensional models of boundary layers are usually more sensitive to such parametrizations than models in which three-dimensional vertical motions are represented explicitly. For many applications, simple first-order gradient models are sufficient, in particular, if the simulation resolves the large eddies directly so that only subgrid-scale turbulence is to be parametrized. If, however, turbulence is strongly influenced by directional forces like buoyancy and if grid scales are not small in comparison to the turbulent mixing length, then more advanced models which close on the basis of second or third order moment equations may be necessary (MELLOR and YAMADA, 1982).

MESOSCOP is designed to incorporate various turbulence parametrizations. At present, versions A and B contain first-order parametrizations (LILLY, 1962),

$$\mathrm{F}^t = -\rho\,(\mathrm{K_M} + \nu)\,\mathrm{D} \quad \text{with} \quad \mathrm{D} = \vec{\mathrm{grad}}(\vec{\mathrm{v}}) + [\vec{\mathrm{grad}}(\vec{\mathrm{v}})]^{\mathrm{T}}$$

$$\vec{\mathrm{f}}^{\,t}_{\mathrm{k}} = -\rho\left(\frac{\mathrm{K_M}}{\mathrm{Pr_k}} + \mu_{\mathrm{k}}\right)\vec{\mathrm{grad}}\,(\psi_{\mathrm{k}}), \tag{27}$$

where D, $\mathrm{K_M}$, ν, μ_k and $\mathrm{Pr_k}$ stand for the deformation tensor, the turbulent mixing coeffient, the molecular viscosity, and the molecular diffusivity and turbulent Prandtl number of scalar ψ_k, respectively. Turbulent mixing is only invoked, where the local Richardson number Ri indicates instability:

$$\mathrm{K_M} = \begin{cases} 0 & \text{if} \quad \mathrm{Ri} \geqslant 1 \\ l_t^2\,\sqrt{(\mathrm{D}^2/2)\,(1-\mathrm{Ri})} & \text{if} \quad \mathrm{Ri} < 1; \quad l_t = \min\,(c_t\,\Delta, l) \end{cases} \tag{28}$$

$$\mathrm{Ri} = -\frac{\sum\limits_{k=1}^{K} \mathrm{A_k}\,\vec{\mathrm{g}} \cdot \vec{\mathrm{grad}}\,\psi_{\mathrm{k}}}{\rho\,\mathrm{D}^2/2} \tag{29}$$

Here c_t is a constant ($c_t = 0.2$ is a common value), Δ denotes the effective grid scale and l stands for a prescribed mixing length. A detailed description of the first order turbulence formulation is given in VOLKERT and SCHUMANN (1986).

MESOSCOP version C applies a second order model (version M2 of FINGER and SCHMIDT, 1986) in which the turbulent kinetic energy E is determined from a transport equation and fluxes are composed of the isotropic contribution from E and anisotropic parts from algebraically approximated second order closure equations. The mixing length l is determined to be the minimum of Blackadar's mixing length scale and a scale accounting for the limitation of upward motion in stratified turbulence. If in this model E is computed such that production and dissipation of kinetic energy are in local equlibrium, then the model reduces to a first-order model with anisotropic diffusion coefficients.

2.7 Representation of Cloud Microphysics

MESOSCOP version A contains parametrizations of cloud formation and precipitation for deep convection in which not only liquid but also ice processes are treated. Since it is important to resolve the three-dimensional dynamics of large convective clouds, we have to select a microphysical model which is simple enough to make such three-dimensional simulations economically feasible. Therefore, instead of particle spectra only a few categories of water particles, where the spectral distribution is expressed solely as a function of the mass content, are considered. At present we use five particle categories: cloud water and cloud ice (frozen cloud droplets, vapour grown plates and slightly rimed plates) moving with the velocity of the air, rainwater and graupel (or hail) representing liquid and solid phase precipitating particles, and snowflakes as a further precipitating category, because snow processes are important for formation of hail embryos. The cloud water and ice is assumed to have a log-normal spectrum. The precipitating particles are assumed to be Marshall-Palmer distributed and fall with their mass weighted terminal velocity $\overline{\mathrm{v}}_{\mathrm{k}}^{\mathrm{term}}$ thus contributing to diffusive fluxes $\vec{\mathrm{f}}^{\mathrm{p}}_{\mathrm{k}}$.

Table 2 List of scalar prognostic model variables ψ_k for cloudy air

k	code	entity
1		entropy
2	V	water vapour
3	C	cloud droplets
4	R	raindrops
5	I	ice crystals
6	G	graupel, spherical hail
7	S	snowflakes

Table 2 lists the different independent variables used to represent clouds; $m^1 = \psi_2$ denotes the vapour concentration, $m^2 = \psi_3 + \psi_4$ represents liquid water and $m^3 = \psi_5 + \psi_6 + \psi_7$ ice water components. The precipitation fluxes are given by

$$\vec{f}_1^p = (s_2 - s_1)(\vec{f}_3^p + \vec{f}_4^p) + (s_3 - s_1)(\vec{f}_5^p + \vec{f}_6^p + \vec{f}_7^p) + (s_1 - s_0) \sum_{k=2}^{7} \vec{f}_k^p$$

$$\vec{f}_k^p = \rho \psi_k \left[\vec{v}_k^{\text{term}} - \sum_{j=2}^{7} \psi_j \vec{v}_j^{\text{term}} \right], k = 2, \ldots, 7 \quad \text{with} \quad \vec{v}_j^{\text{term}} = 0 \quad \text{for} \quad j = 2, 3, 5. \tag{30}$$

This incorporates the constraint that the sum over all precipitational fluxes of air components vanishes. Conversion processes are represented in the model by proper parametrizations for the sources q_k. The present model describes the processes indicated in Figure 2. For example, seven individual processes contribute to q_3 for cloud water. Condensation of cloud droplets is treated implicitly to achieve water saturation adjustment (see Appendix B). All other microphysical processes are calculated explicitly using

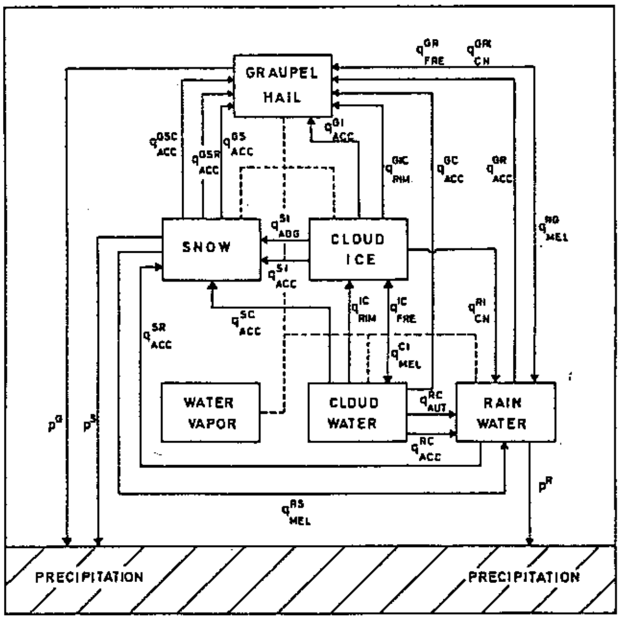

Figure 2
Schematic diagram of the different kinds of particles, condensation and sublimation processes (dashed), other microphysical processes q and the precipitation fallout p. Upper index group: kinds of particles involved, abbreviation codes as in Table 2. Lower index: microphysical process, where AUT: autoconversion; ACC: accretion; RIM: riming; FRE: freezing; CN: contact nucleation; MEL: melting.

parametrizations of the transformation rates. The evaporation of rain, sublimation of graupel and snow, freezing of cloud droplets and rain, accretion processes for graupel and snow, aggregation of snow and melting of ice particles are described by rate equations similar to those of LIN et al. (1983) or WISNER et al. (1972). The depositional growth rate of ice crystals is computed from the values of KOENIG (1971). The autoconversion and accretion processes of droplets, the riming rate of ice crystals and the subsequent growth of these crystals into graupel are treated following HÖLLER (1986), which also contains a detailed description of all microphysical processes.

2.8 Some Key Technical Features

Once the model equations have been chosen and the numerical algorithm is designed, there is still a considerable amount of work in mapping these ideas onto a computer system. Here, we want to briefly summarize some key technical features.

Segmentation of data in vertical x/z-slabs is systematically used to allow for data transfer on disks if the central memory of the computer cannot contain all three-dimensional fields at the same time. This enables us to deal with grids of up to 64^3 cells on computers with approximately 10^6 words of central memory (e.g. CRAY-1/S). A 'back slide' structure within the algorithm for the direction normal to the data slabs minimizes the number of time consuming input/output operations (details in VOLKERT and SCHUMANN, 1985). The decision, whether to use external storage or not is made automatically at the expense of an additional program level for data management above the level of formula evaluation. A combination of synchronous and asynchronous input/output software ensures that the time for transfers is less than the time for calculations. The code is highly vectorized for CRAY compilers. Software tools are used to maintain the program.

3 Validation Examples

In this section we present five validation examples for the three versions of MESOSCOP. These deal in sequence with a rising thermal, gravity waves over mountains, the retardation of a cold front at a mountain, a convective boundary layer and with cumulus cloud convection. The examples are chosen in such a way that sufficient information is available for the purpose of validation and that all essential features of MESOSCOP can be demonstrated, as indicated in Table 4. In turn, the five cases are compared to self-similarity and conservation properties, exact analytical solutions exhibiting constant vertical transport of momentum, approximate analytical and numerical reference solutions, measurements in the laboratory and atmospheric field observations. For each case, we sequentially introduce the physical problem, explain the reference information that is used to compare with the model results, state the specific parameters of the model simulations and report on the results of the comparisons.

3.1 Self-Similarity of a Rising Thermal

A 'thermal' is a finite volume of buoyant (light) fluid rising in an ambient fluid. Much is known about thermals from previous studies, e.g. by SCORER (1958), LILLY (1962, 1964), OGURA (1962), DALEY and MERILEES (1971) and FOX (1972). In particular, it has been shown that a turbulent thermal develops into a self-similar state, in which its parameters vary as fractional powers of time and height. Theories exist also for the case without any diffusion (DALEY and MERILEES, 1971) with which we can make comparisons. Thus, it becomes a challenge to show whether MESOSCOP is capable of simulating the dynamics of a thermal in accordance with existing theories.

We consider an initially small volume of lighter fluid near the lower boundary of a three-dimensional computational 'box', which rises upwards after sudden release. We look for the self-similar state when an equilibrium between inertia, buoyancy and mixing is achieved, but before the thermal gets influenced by the top or side boundaries of the box. This approach is similar to that used by OGURA (1962) and DALEY and MERILEES (1971), who consider an axially symmetrical thermal in a two-dimensional simulation. The grid spacings used are those of OGURA (1962) but in three dimensions. Like FOX (1972) we make use of the symmetry of the problem with respect to the vertical axis of the thermal by simulating only one-quarter of the whole domain. Preliminary tests with a thermal in the centre made sure that the code preserves symmetry.

Self-similarity develops if the thermal rises in an uniform, incompressible fluid far away from any boundary, if its density differs only little from that of the ambient fluid and if mixing with the environment is controlled by the same scales as those of the shape of the thermal (LILLY, 1964). In this state, dimensional arguments (SCORER, 1958) show that the effective radius R, the maximum vertical velocity w_m, the maximum temperature surplus θ'_m (if temperature causes the density difference), and the heights h_w, h_θ of the velocity and temperature maxima are related to time by

$$R \sim t^{1/2}, w_m \sim t^{-1/2}, \theta'_m \sim t^{-3/2}, h_w \sim h_\theta \sim t^{1/2}, \tag{31}$$

Therefore, we consider a thermal of initial radius R_* within a Boussinesq fluid initially at rest in a box of size $0 \leqslant x \leqslant 10\, R_*$, $0 \leqslant y \leqslant 10\, R_*$, $0 \leqslant z \leqslant 15\, R_*$. Buoyancy $g\rho'$ is due to a temperature surplus θ' with $\rho' = -\rho\theta'/\theta_0$. The initial temperature distribution is specified following OGURA (1962); θ' vanishes everywhere except for

$$0 \leqslant z < 2\, R_* \quad \text{where} \quad \theta' = \theta_* \exp\left[-2.3\left(\frac{r}{R_*}\right)^2\right] \sin^2\left[\frac{\pi z}{2\, R_*}\right], \quad r = \sqrt{x^2 + y^2}. \tag{32}$$

In the program one scalar $\psi_1 = \bar{\theta} + \theta'$ is integrated (K = 1). The value of $\bar{\theta}$ is physically arbitrary, but does influence the numerical accuracy because of the non-linear properties of the Smolarkiewicz-scheme used for advection of scalars. Two cases are considered ($\bar{\theta} = 0$ and $\bar{\theta} = 300\, \theta_*$). The actual values of R_*, θ_*, g and θ_0 do not matter. We use $w_* = (2R_*\theta_* g/\theta_0)^{1/2}$, R_* and θ_* to present results in non-dimensional form; $t^* = t\, w_*/R_*$ is the non-dimensional time. All boundaries are specified to be impermeable, frictionless and adiabatic (type CLOS). The grid spacings are $\Delta x = \Delta y = \Delta z = R_*/3$; i.e. initially the resolution is coarse. The time step amounts to $\Delta t = 0.15\, R_*/w_*$, which has been found to be sufficient for numerical stability.

First, we consider an inviscid simulation without any physical diffusion ($K_M = 0$) in order to check the conservation properties of the numerical method. In particular we require that the volume integrals of density ρ, temperature θ and momentum $\rho\vec{v}$ stay constant. Without diffusion, also quadratic quantities like total energy being composed of kinetic and potential energies and the temperature variance

$$E_{kin} = \iiint \frac{\rho \vec{v}^2}{2}\, dV; \qquad E_{pot} = \iiint g\, z\, \rho'\, dV, \qquad E_\theta = \iiint \frac{\theta'^2}{2}\, dV \tag{33}$$

should stay constant, where the integrals are taken over the computational domain. As long as the resolution is fine enough to represent temperature and velocity in the rising and deforming lighter fluid without approximation errors, the maximum value θ'_m of the temperature should also stay constant, and the vertical velocity w_m should increase linearly with time as long as the thermal is far away from boundaries, because $d\theta'/dt = 0$ and $dw/dt = g\,\theta'/\theta_0$ in this case.

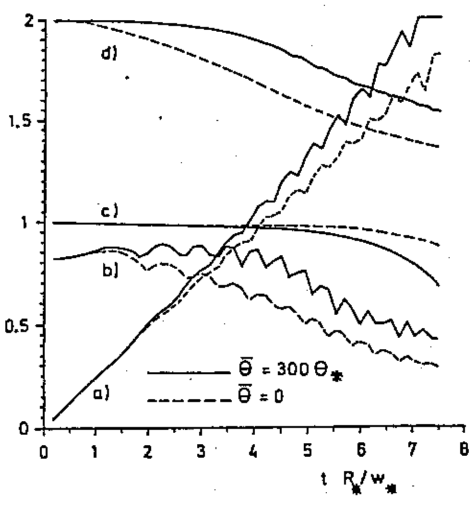

Figure 3

Parameters of a thermal rising with zero diffusivities versus time. a) w_m/w_*; b) θ'_m/θ_*; c) $(E_{kin} + E_{pot})/E_{pot}$ $(t = 0)$; d) $1 + E_\theta/E_\theta$ $(t = 0)$. Full lines for $\overline{\theta} = 300\,\theta_*$; dashed lines for $\overline{\theta} = 0$.

Inviscid results are collected in Figure 3. They show that w_m increases approximately linearly with time, total energy remains fairly constant for some time, while maximum temperature and temperature variance stay not quite so constant. Note that initially the thermal extends over only 6 grid cells so that resolution is poor and the present case forms a strict test for the accuracy of the numerical scheme. Small oscillations in θ'_m arise simply because the location of the maximum temperature only sometimes coincides with grid points but otherwise falls inbetween, and hence cannot be resolved exactly. Because of the increasing velocity, the numerical stability limit $\Delta t\, w_m/\Delta z \leqslant 0.5$ is reached at $t^* = 4.5$. However, the solution stays stable till $t^* = 9$. Two different values of $\overline{\theta}$ are used. For $\overline{\theta} = 0$, the advection scheme guarantees positivity of the temperature surplus but obviously this advantage has to be paid for by increased numerical diffusion causing early decreases of θ'_m, E_θ, and w_m. Still, the numerical diffusion effects are small. This can be seen from the fact that the velocity comes close to the value $w_m/w_* = 2$ at $t^* = 7.5$ while it amounts to only 0.75 if physical diffusion is included as described below. For $\overline{\theta} = 300\,\theta_*$ the numerical diffusion is even smaller. In spite of the coarse resolution, total energy is conserved to within 4 % in the initial period ($t^* \leqslant 4.5$) where the stability restriction is satisfied. Linear quantities like volume integrals of density, momentum and temperature are conserved up to round-off errors (not plotted).

Now, we turn to the turbulent case. Mixing is modelled by using the first-order turbulence model (Equation 27), without molecular contributions, $c_t = 0.2$. To reduce the number of independent parameters, we set $Ri \equiv 0$. Since the mixing length has to be proportional to the radius of the thermal, we set

$$l_t = 0.5\,R, \qquad R = \left(\frac{3V}{4\pi}\right)^{1/3}, \qquad V = E_{kin}\Big/\left(\frac{3}{2}\rho w_m^2\right). \tag{34}$$

The turbulent Prandtl number is unity and $\overline{\theta} = 300\,\theta_*$. After a time of order R_*/w_* the thermal has climbed so far from the lower boundary that its influence is negligible. A much longer time, of order $R^2/K_M = 16$ is required to achieve equilibrium between inertia, buoyancy and friction. Figure 4 shows the shape of the thermal as represented by contours of constant temperature in a plane of symmetry. The similarity in shape of the results at $t^* = 22.5$ and $t^* = 45$ indicates that the self-similar state is reached. As has been seen in previous simulations (e.g. FOX, 1972) and experiments (SCORER, 1958), a mushroom shape is formed. The temperature gradient is steep at the top of the thermal because of large buoyancy accelerations below this border.

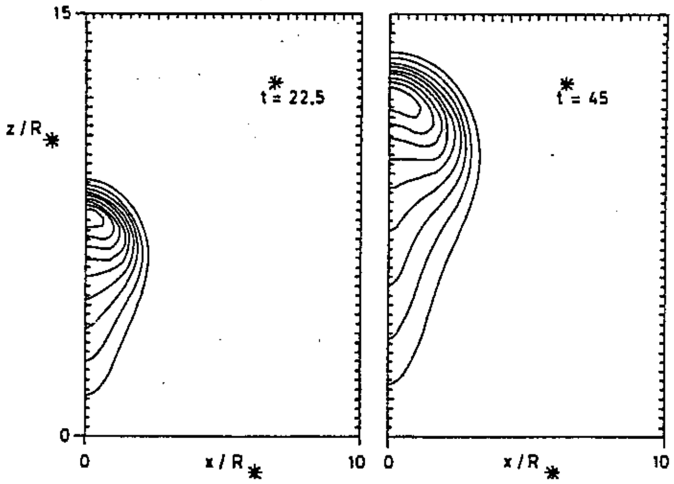

Figure 4 Temperature contours of a diffusive thermal approximately in self-similarity state at the indicated times. Isoline increment: $\theta'_m/10$.

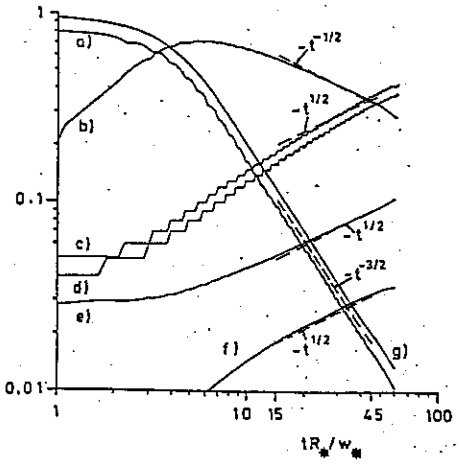

Figure 5 Parameters of a diffusive thermal versus time. a) θ'_m/θ_*; b) w_m/w_*; c) $h_\theta/(300\,R_*)$; d) $h_w/(300\,R_*)$; e) $R/(10\,R_*)$; f) $E_{kin}/(100\,E_{pot}(t=0))$; g) $E_\theta/E_\theta\,(t=0)$. The straight dashed lines indicate the expected trends in the self-similarity state.

In Figure 5, the quanitities addressed in Equation (31) are plotted on logarithmic scales so that they should vary linearly in the self-similar state. Small oscillations or step-wise variations at early times are due to the initially coarse discrete representation of the fields. The figure reveals that self-similarity is reached for $15 \leqslant t^* \leqslant 45$. As in previous studies, temperature achieves self-similarity first, followed by velocity and length scales. The self-similarity of the length scales is sowewhat obscured by the fact that the virtual origin is not zero. At later times, the motion of the thermal is influenced by the top boundary which explains the observed deviations for $t^* \geqslant 45$. Also included in this figure are the results for second order integrals E_{kin} and E_θ, defined in Equation (33), for which dimensional analysis predicts

$$E_{kin} \sim t^{1/2}, \quad E_\theta \sim t^{-3/2}. \tag{35}$$

We see that these integrals conform with the expected trends even better than the local values which are influenced more strongly by numerical approximation errors. The slope values computed from the results at the limits of the interval $15 \leqslant t^* \leqslant 45$ are -1.488, -0.45, 0.63, 0.63, 0.48, 0.53, -1.508 for the curves a) to g) of Figure 5, respectively. The difference to the corresponding theoretical value is less than 0.13 and amounts to 0.008 for temperature variance. In view of the limited variance conservation properties of the scalar advection scheme, the agreement for E_θ is particularly satisfactory.

In contrast to OGURA (1962), whose results are a pure consequence of numerical diffusion (he did not include any physical diffusion explicitly and his results for maximum velocity show a slower decrease), our results are only weakly influenced by numerical approximation errors.

3.2 Gravity Waves in an Idealized Airflow over Bell-Shaped Mountains

The generation of internal gravity waves in an stably stratified atmosphere which flows over mountains is a thoroughly studied topic of mesoscale meteorology (see SMITH, 1979, for a review). The resultant vertical transport of horizontal momentum can have an important impact on both smaller scales (e.g. through strong downslope winds) and larger ones (e.g. by affecting the synoptic scale momentum budget).

The highly idealized situation of a two-dimensional, steady, inviscid, hydrostatic and Boussinesq flow with constant inflow velocity and uniform stratification over a bell shaped mountain is a special case of Long's problem, for which analytical solutions exist even for the non-linear case of finite mountain height. In this section we demonstrate to what extent the version of MESOSCOP with terrain following coordinates is able to reproduce these reference solutions. Dry air is considered in the Boussinesq approximation with constant reference density $\bar{\rho}$ and with potential temperature as the only scalar (cf. Equations 1 to 3; $K = 1$; $\psi_1 \equiv \theta$).

LILLY and KLEMP (1979) show that hydrostatic flows, idealized as mentioned above, are solutions of the linear differential equation

$$\left(\frac{\partial^2}{\partial z^2} + m^2\right) \delta = 0, \qquad m = \frac{N}{U} \tag{36}$$

for the vertical displacement $\delta(x, z)$ of an air parcel from its undisturbed height (far upstream) $\bar{z}$, i.e. $\delta = z - \bar{z}$. The vertical wave number m relates the constant inflow velocity U and the constant Brunt-Väisälä frequency $N = [g/\theta_0 \cdot \partial\theta/\partial z]^{1/2}$. The velocity components u and w and the potential temperature θ are connected to δ via

$$u = U\left(1 - \frac{\partial\delta}{\partial z}\right), \quad w = U\frac{\partial\delta}{\partial x}, \qquad \theta = \theta_0\left[1 + \frac{N^2}{g}\ (z - \delta)\right], \tag{37}$$

where θ_0 and g denote the Boussinesq reference value for θ (e.g. $\theta_0 = 290$ K at the ground) and the acceleration of gravity, respectively. Equation (36) is solved for δ, assuming a radiation boundary condition at the model top and a free slip condition at the ground, via numerical integration of Fourier integrals for several analytic surface elevation profiles $z_s(x)$. We consider a bell shaped mountain $[z_s(x) = h/(1 + x^2/a^2)]$ with summit height h and half-width a, for which JANK (1984) describes the mathematical and numerical procedure in detail (following LILLY and KLEMP, 1979).

The present problem is governed by two dimensionless quantities, $m \cdot h$ and $m \cdot a$. If $m \cdot h \ll 1$ the flow is essentially linear; non-linear effects become important when $m \cdot h \approx 1$, while $m \cdot h = 0.85$ constitutes the threshold above which streamlines overturn in the hydrostatic limit (supercritical flows). If $m \cdot a \gg 1$ the flow is virtually hydrostatic, whereas non-hydrostatic effects become important when $m \cdot a \approx 1$.

Our demonstration cases deal with a constant vertical wavenumber ($m = 2\pi \times 10^{-4}\ m^{-1}$; $N = 4\pi \times 10^{-3}\ s^{-1}$; $U = 20$ m/s) and the domain parameters (lateral and vertical extensions L and H, respective grid spacings Δx and Δz) as given in Table 3; the summit height h is varied in order to obtain a quasi linear and a non-linear (but subcritical) quasi-hydrostatic situation. The hill is centred between the inflow and outflow boundaries.

For verification, steady numerical results are imposed on the hydrostatic reference solution described above. The left part of Figure 6 depicts the vertical velocity component w for experiment LI at normalized time $t^* = t\ U/a = 100$. The updraft and downdraft regions above the very flat, but broad hill coincide nearly perfectly. Another important feature lies in the illustration of the inevitably imperfect formulation of boundary conditions for limited area models. The BKD condition (cf. Section 2.3)

Table 3 Physical parameters m, h, a and derived domain parameters L, Δx, z_t, Δz for a quasi-linear (LI) and a nonlinear (NL) numerical experiment (symbols are explained in the text; blank entries denote repetition of value above)

Exp.	m (1/m)	h (m)	a (m)	L	Δx	z_t	Δz
LI	$2\pi \times 10^{-4}$	10	5×10^4	24a	L/120	$3\pi/m$	$z_t/60$
NL		10^3			L/60		$z_t/30$

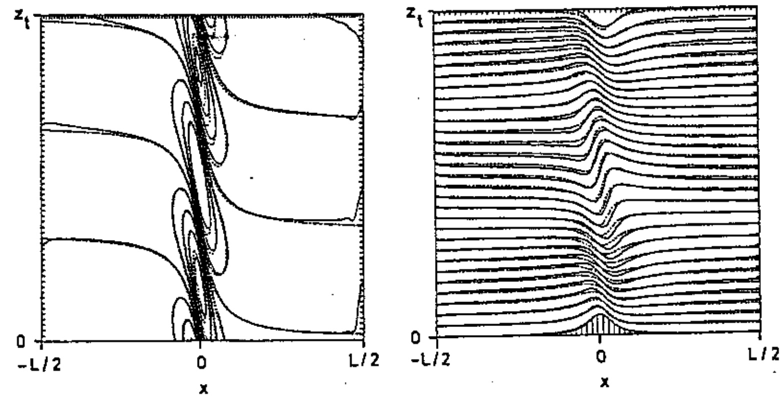

Figure 6
Comparison of numerical results (solid) and reference solution (dashed). Left: vertical velocity component w for the linear cases LI (see Table 3; isoline increment: U/25000;normalized model time t* = 100); right: streamlines in terms of potential temperature for the non-linear case NL (see Table 3; isoline increment: $N^2\theta_0\Delta z/g = 2.33$ K; isoline range: from $\theta_0 = 290$ K (ground) to 360 K (top); normalized model time t* = 80).

yields quite satisfactory transports through the open top boundary whereas the boundary conditions at the side (FLUX at inflow, RADI at outflow) are not able to prevent kinks in the zero lines of w.

Streamlines in terms of potential temperature in the steady state are depicted in the right part of Figure 6 for the non-linear experiment NL and imposed on the reference solution. The isoline increment is equivalent to a tenth of the vertical wavelength or to two vertical gridsizes. The figure shows a high conformity between numerical and reference solution, though systematic differences are evident. Differences are smallest at multiples of half a vertical wavelength, while in between, systematic positive and negative deviations occur on the upstream (left) side of the ridge which vanish only at the boundary due to fixed inflow values. Over the ridge the simulated wave exhibits a slightly larger amplitude than the reference solution, especially at streamlines which commence at heights between multiples of half a vertical wavelength. At the downstream boundary we find the same systematic height dependence of differences as at the upstream boundary, but streamlines are horizontal due to a zero-gradient boundary condition (OUTF) used in this case.

Mountain waves transport horizontal momentum ρu vertically. Besides its physical significance, the momentum flux M provides a sensitve measure for the evaluation of model results. We define it as average over the horizontal extent of the domain along the line $\sigma = \overline{z}$:

$$M(\overline{z}) = \frac{1}{\xi(L/2) - \xi(-L/2)} \int_{\xi(-L/2)}^{\xi(L/2)} [(u - U)\, a^3 + VG^{31} p']\, d\xi. \tag{38}$$

The first summand describes advective momentum flux due to a^3 normal to the curve σ = const., while the second summand includes the horizontal component of the pressure force acting on such a curve, which vanishes in the absence of orography. The expression (u − U) is used instead of u because this

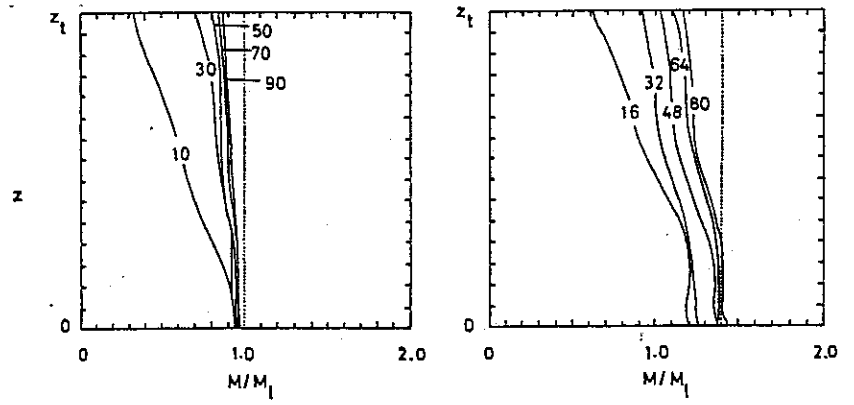

Figure 7
Time evolution of the momentum flux profiles for experiments LI (left) and NL (right) at the indicated normalized times t*; the dashed lines indicate the reference values M_r.

reduces numerical errors if the integral over a^3 is not exactly zero as it should be. We note that the definition given avoids interpolations in the numerical model and that it is defined for all values of $\bar{z}$. At the ground ($\sigma = 0$) the component a^3 vanishes and the pressure term reduces M to the negative surface pressure drag. The momentum flux of the reference solution is independent of height:

$$M_r = f_{nl}\, M_l = - f_{nl} \frac{\pi}{4} \frac{\bar{\rho}\, N\, U\, h^2}{L} \quad , \tag{39}$$

under the assumption that the boundaries of the interval L are far from the ridge. In the linear case the factor f_{nl} equals unity; the reference solution determines f_{nl} as 1.395 in the non-linear case.

Figure 7 shows the vertical distribution of the simulated momentum flux at several nondimensional times t*; the fluxes are normalized by the linear reference value M_l and compared with M_r (dashed). In the linear case LI the flux develops over 50 units of a/U to a steady profile, which is very close to the reference value at the ground and 10 % below it at the top. In the non-linear case NL the steady profile at t* = 80 coincides with the reference value for half a vertical wavelength; higher up it gradually decreases, reaching 85 % of that value at the top.

In summary, MESOSCOP in terrain following coordinates produces results, which in the special case of the hydrostatic Long-problem come close to the 'practical limit of the accuracy of model calculations' (DURRAN and KLEMP, 1983). This is particularly encouraging as no explicit dissipation is used, and no resource consuming damping layer is employed in the upper part of the model domain. We note that Figure 6 shows the entire computational domain. Comparisons with published results from similar test cases (e.g. CLARK and PELTIER, 1977; MAHRER and PIELKE, 1978; KLEMP and LILLY, 1978; DURRAN and KLEMP, 1983; HOINKA, 1985; NICKERSON et al., 1986; FRENZEN et al., 1987) reveal that the simulations presented here are of similar quality as what we consider to be the best result (DURRAN and KLEMP).

3.3 Retardation of an Idealized Cold Front by a Mountain Ridge

The effect of orography on cold fronts has been of increasing interest within mesoscale meteorology during recent years. Cold fronts undergo deformation as they cross large mountains. STEINACKER (1981) has analysed an example with severe deformation. A few more cases have been investigated in detail during the ALPEX observation period. SMITH (1986) summarizes the available results for the Alps and other mountains. Only few theoretical studies have been performed. DAVIES (1984) considers an idealized model of a cold front moving over a mountain ridge under the assumption of geostrophic equilibrium. HADERLEIN (1986) treats the same situation numerically in one and two horizontal dimensions without that assumption.

In this section we use the models of DAVIES and HADERLEIN to check the accuracy of MESOSCOP in terrain following coordinates including Coriolis forces. We simulate a shallow water flow by means of the Boussinesq variant of the complete primitive equations (cf. Equations 1 to 3; $K = 1$; $\psi_1 \equiv \theta$ denoting potential temperature, $\bar{\rho} = \text{const.}$). Numerically this constitutes a nontrivial problem because Davies' model implies a discontinuous vertical temperature profile with a temperature step. Furthermore, the tangential velocity is discontinous at the frontal interface.

Both DAVIES and HADERLEIN consider a shallow-water flow model on a f-plane, where a 'free surface' $h(x, t)$ represents the interface between cold air below and warm air above, as sketched in Figure 8. The cold air is assumed to have uniform density and flows with vertically uniform velocity u normal to the front and v parallel to the front. The constant potential temperature θ of the cold air differs from the temperature θ_0 of the overlying warm air by $\Delta\theta$. Friction forces are neglected. The flow is barotropic and driven by a geostrophic pressure gradient $(-f\rho_0 V_g, f\rho_0 U_g)$ horizontally and exposed to the reduced gravity $g' = g\,\Delta\theta/\theta_0$ vertically. H_F designates the asymptotic height of the front at infinity $(x \to -\infty)$. As potential vorticity is conserved $[(f + \partial v/\partial x)/h = f/H_F]$, the front moves quasi-stationarily over flat terrain with the geostrophic wind U_g in the horizontal direction normal to the front. For $t \leqslant 0$, i.e. before the front reaches the mountain, the height of the front is given by (DAVIES, 1984):

$$h(x, t) = H_F\,[1 - \exp\{(x - U_g t)/R\}]. \tag{40}$$

Here $R = C/f$, and $C = (g' H_F)^{1/2}$ stand for the Rossby radius and the gravity wave speed, respectively. Over flat terrain, the velocity v parallel to the front is $v = V_g$ in the warm air and

$$v(x, t) = V_g - C \exp\{(x - U_g t)/R\} \tag{41}$$

in the cold air.

DAVIES has considered this wedge of cold air approaching an infinitely long orographic ridge with maximum height H_B, width L and the profile

$$z_s(x) = H_B \sin^2\left(\frac{\pi x}{L}\right) \quad \text{for} \quad 0 \leqslant x \leqslant L; \quad z_s(x) = 0 \quad \text{elsewhere.} \tag{42}$$

Under the assumption of semi-geostrophic equilibrium, i.e. $|du/dt| \ll |f(v - V_g)|$, an analytical solution exists for the elevation $h(x, t)$ of the front for $t > 0$.

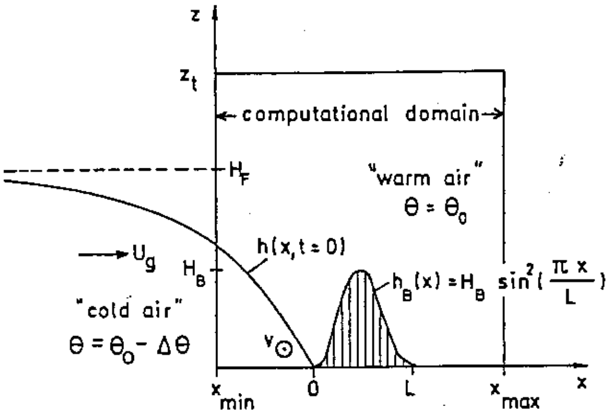

Figure 8
Sketch of the idealized cold front approaching a two-dimensional mountain ridge, and of the computational domain.

MESOSCOP in terrain following coordinates is used to calculate the flow within the computational domain shown in Figure 8 with $x_{min} = -L$, $x_{max} = L$ and $z_t = 1.6\ H_F$. The quasi-stationary solution given in Equations (40, 41) is used to specify the initial conditions and the inflow boundary conditions, i.e. we prescribe $u = U_g$ and

$$\phi = \gamma\,\phi_C + (1-\gamma)\,\phi_W, \quad \phi = v, \theta, \tag{43}$$

where ϕ_C is the value valid for $z < h(x, t)$ in the cold air and ϕ_W the value for $z > h(x, t)$ in the warm air. Ideally, the weight $\gamma = \gamma(x, z, t)$ is unity in the cold air and zero above. In order to avoid a stepwise variation of the height of the frontal interface, however, a linear interpolation is used in the mesh cells adjacent to the interface according to

$$\gamma = \min\{1, \max(0, [h(x,t) - z_{k-1/2}]/\Delta z_k)\}, \quad \text{with} \quad \Delta z_k = z_{k+1/2} - z_{k-1/2}, \tag{44}$$

where $z_{k+1/2}$ and Δz_k denote the height of the mesh cell boundary between grid points with indices k and k + 1 and the vertical mesh spacing, respectively.

The initial field is adjusted by a solution of Poisson's equation in order to make it non-divergent (see Appendix B). At the top an open boundary with constant pressure is prescribed (OUTF). At the outflow boundary the Sommerfeld radiation condition is applied (RAD1). A test without any mountain has shown that the numerical implementation of this boundary conditions causes negligible disturbances (SCHUMANN, 1987b).

For comparison we consider a case for which the numerical solution of HADERLEIN is available: $H_B = 2$ km, $L = 250$ km, $H_F = 8$ km, $\Delta\theta = 6$ K, $\theta_0 = 300$ K, $U_g = 20$ m/s, $V_g = 10$ m/s, $f = 10^{-4}\,s^{-1}$, $g = 10\ ms^{-2}$. These parameters imply a gravity wave-speed of $C = 40$ m/s and a Rossby radius of $R = 400$ km. The computational domain is equidistantly divided into 96 grid cells horizontally and 40 grid cells vertically. The time step has to be rather small because of large vertical velocities; it is set to $\Delta t = 0.1\ \Delta x/C$.

Figure 9 shows results for a sequence of non-dimensional times $t^* = tU_g/L$ in comparison to HADERLEIN's and DAVIES's results. Note the different scales in horizontal and vertical directions. The shallow water solution of DAVIES is shown only for early times, because negative values result for $t^* > 0.885$ with the present parameters. This limitation is a consequence of the semi-geostrophic approximation.

Both the present and HADERLEIN's method predict a frontal interface which experiences an upwelling at the upslope side of the mountain. This upwelling gradually leads to a hydraulic jump, which moves upstream as the gravity-wave speed C is large compared to the fluid's velocity U_g. A hydraulic jump is to be expected, if one applies the theory of HOUGHTON and KASAHARA (1968) to the present flow, which

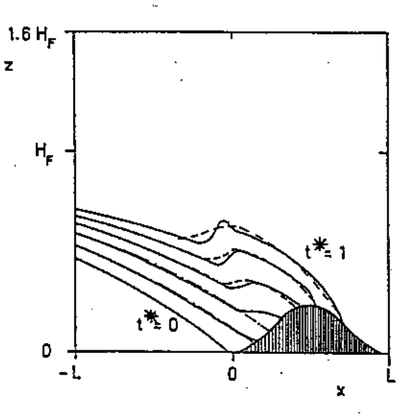

Figure 9 Isochrones of the frontal interface in a vertical plane at times $t^* = 0, 0.2, 0.4, 0.6, 0.8, 1.0$. Comparison of MESOSCOP results (contours of $\theta_0 - \Delta\theta/2$; full lines), results from a shallow water equation model (HADERLEIN 1986; dashed lines) and analytical theory (DAVIES 1984; dash-dotted lines).

is governed by a Froude number $F = U_g/C = 0.5$. The results seem to indicate that the present model has less numerical diffusion for the jump than HADERLEIN's. The frontal interface upstream the hydraulic jump is unaffected and corresponds to the quasistationary solution of Equation (40).

DAVIES's solution does not show a jump. This is a consequence of the semi-geostrophic assumption which is valid only for $U_g^2 R/(C^2 L) \ll 1$. In the present situation this ratio is 0.4. Thus, DAVIES's solution is valid for cases with $C \gg U_g$ (if $L \approx R$), where disturbances induced by the mountain propagate upstream very quickly. Such extreme cases are rare in reality.

The comparison shows that the inertia of the warm air, which is included in the present model but neglected in the models of DAVIES and HADERLEIN has only a little effect on the cases discussed. The vertical inertia would be important for non-hydrostatic flow situations. Moreover, the comparison supports the validity of the present model and shows that it can be applied to investigate the retardation of a cold front by a mountain. Further cases, both in two and three dimensions including also the effect of stable stratification and comparisons with observations have been studied and are reported elsewhere (SCHUMANN, 1987b).

3.4 Large Eddy Simulation of a Turbulent Convective Boundary Layer

Turbulence in the convective boundary layer (CBL) is driven by upward heat flux from the ground while contributions from wind shear are negligible (WYNGAARD, 1985). Parametrization of turbulence in such a layer is difficult and subject of ongoing research; it has to include the buoyancy forcing. First- and second-order ensemble averaged turbulence models cannot account for the flowfield structures which are characteristic for the CBL like strong upward motions in isolated thermals and slow downward motions in the surroundings. In this section we focus resolution on the details of turbulent convection, reducing the width of the numerical grid to the scale of eddies in the inertial subrange of turbulence. Most of the turbulent kinetic energy is resolved, whereas the subgrid scale fluxes are modelled by either second or first order closure. This technique is termed large eddy simulation (LES), see e.g. SCHUMANN and FRIEDRICH (1986).

In order to validate this approach, we apply the method in the Boussinesq approximation with $\bar{\rho}$ = const. to the CBL, which has been investigated by DEARDORFF and WILLIS (1985), from now on referred to as DW85, in a laboratory experiment. A water tank with initially stable stratification is heated from below. DW85 measured profiles and spectra of turbulence quantities, to which we can compare numerical results.

The water tank is 1.24 m long and wide and filled up to 0.4 m with water. The initial temperature varies smoothly from 20 °C at the bottom to 32.5 °C at the water surface. The bottom of the tank is heated at a constant rate with a kinematic heat flux $Q_0 = 1.4 \times 10^{-3}$ Km/s. This causes a CBL from the bottom up to a depth z_i, which slowly increases with time. From these parameters one defines convective velocity and temperature scales (WYNGAARD, 1985)

$$w_* = (\beta\, g\, Q_0\, z_i)^{1/3}, \quad T_* = \frac{Q_0}{w_*}, \tag{45}$$

where the volumetric expansion coefficient is $\beta = 2.3 \times 10^{-4}\ \mathrm{K}^{-1}$. These scales depend on time because of variable height z_i. Evaluating them for the height of the water tank ($z_t = 0.4$ m), gives scales $w^* = 1.08 \times 10^{-2}$ m/s, $T^* = 0.13$ K, which characterize the order of magnitude of scales to be expected. The measured spectrum of turbulent kinetic energy indicates that the peak wavelength is of order z_i while the inertial subrange starts at a normalized wavenumber $k_h z_i$ of order ten (see Figure 10). The latter value gives the required grid scales, while the peak wavelength determines the minimum horizontal extent of the computational domain. Computer memory restrictions prevent the whole tank being

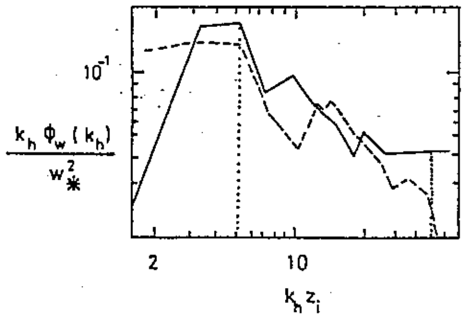

- **Figure 10**
  Vertical velocity spectra versus normalized horizontal wave number. Dashed curve from DW85 for $z/z_i = 0.62$, solid curve from LES for $z/z_i = 0.64$. The inertial subrange (marked by the dotted lines) covers wavenumbers $5 < k_h z_i < 50$.

modelled. We use $\Delta x = \Delta y = \Delta z = z_t/40$ and a computational domain extending over 60 x 60 grid cells horizontally with periodic lateral boundary conditions (PERI) and 40 cells in the vertical. This limits the simulation to the time period where the height of the convective layer z_i remains less than the horizontal and vertical extent of the computational domain. At the bottom we use no-slip boundary conditions for the velocities and prescribe the flux Q_0 for the temperature equation (FLUX). At the top boundary, the boundary condition OUTF is applied in order to avoid reflection of gravity waves which might cause spurious oscillations in the upper stable layer.

Subgrid scale fluxes are parametrized by the second order model as sketched in section 2.6; two scalars (K = 2) are used: ψ_1 representing temperature and ψ_2 the subgrid-scale kinetic energy. The time step Δt is initialized with an arbitrary initial value and then adjusted such that it falls between 50 to 100 % of the maximum time step permitted by numerical stability (see Section 2.3). Initial conditions prescribe the temperature according to the measured temperature profile, velocities are set to zero except for the vertical component which is initialized with random numbers of amplitude w^*. The velocity fields are corrected to satisfy continuity as described in Appendix B. The initial subgrid-scale kinetic energy varies with height as $w^{*2}(1 - z/z_t)$. The integration runs over 1523 time steps up to t = 191 s, for which time DW85 give their first results. This time is large in comparison to the characteristic turnover-time scale $z_i/w_* = 21.7$ s of the dominant thermals.

Figure 11 shows a vertical (x/z) cross-section of vertical velocity w for t = 191 s where $z_i = 0.45\, z_t$. The CBL is contained in the domain with strong updrafts and downdrafts whereas the velocities are small in the stable layer aloft. The vertical profile of vertical velocity variance $\overline{w^2}$ versus z/z_i has its

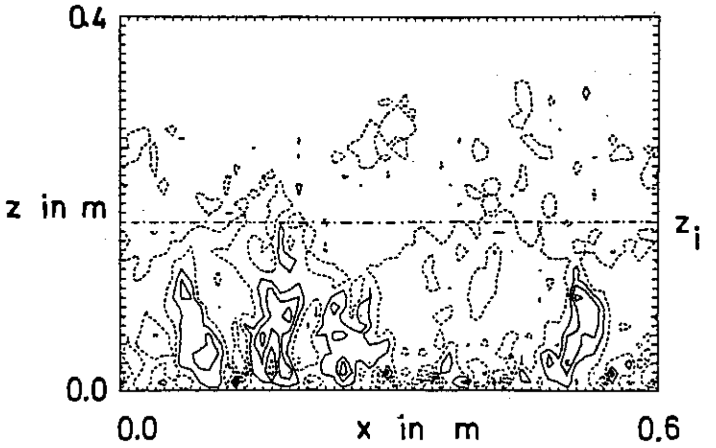

- **Figure 11**
  Vertical velocity component w in a x–z cross section at t = 191 s. Isoline increment: $0.5w_*$; solid (dashed) lines represent positive (negative) values; z_i denotes the inversion height.

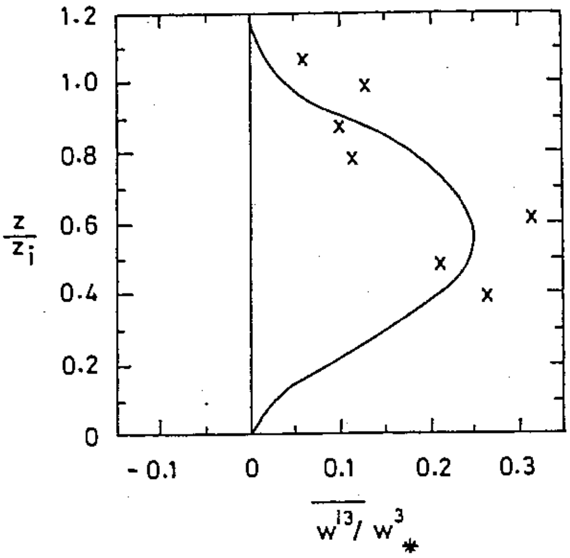

- Figure 12 Vertical profile of $\overline{w'^3}/w_*^3$; solid curve from LES, crosses from DW85.

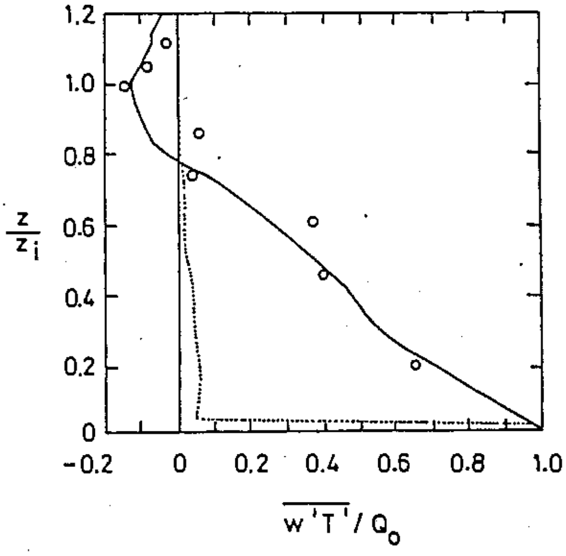

- Figure 13 Vertical profiles of the ratio turbulent heat flux $\overline{w'T'}$ to surface flux Q_0: measured (from DW85; circles) and calculated by LES for t = 191 s (solid line). The dotted line indicates the subgrid scale portion of the calculated flux ratio.

maximum value of $0.38\ w_*^2$ at $z/z_i = 0.47$. This agrees well with the measurements of DW85 (maximum 0.34 at $z/z_i = 0.42$). The maximum computed updrafts are more concentrated and exhibit larger vertical velocity magnitudes than the downdrafts. This results in a non-Gaussian velocity distribution with non-zero skewness $\overline{w^3}$ as plotted in Figure 12. The vertical heat flux is shown in Figure 13 in comparison to the measured data. The subgrid scale flux decreases rapidly above the lower boundary. The simulation is indeed a LES as it resolves more than 90 % of the heat flux carrying eddies or thermals. The total heat flux decreases with height approximately linearly. Its vertical divergence causes the warming of the layer below the inversion height. Near the inversion the flux shows negative values due to entrainment processes in accordance with the measurements. At heights $0.5 \leqslant z/z_i \leqslant 0.8$ both the heat flux and the vertical temperature gradient are positive. This is, therefore, a region of countergradient heat flux. The origin of such a countergradient flux has been explained for the present and other cases by SCHUMANN (1987a).

The results are sensitive to resolution as must be expected. For larger grid spacings $(z_t/20)$, the subgrid scale transports become comparable in magnitude to the resolved fluxes. Simulations with the second order model were compared with the related first-order model (cf. section 2.6). The results show that the first-order model overestimates the negative heat flux near the inversion and smoothes the temperature profile in this domain whereas the second order model simulates a sharp inversion even with the coarser resolution.

From the LES results, a computation was made of the spectrum $\phi_w(k_h)$ of horizontal variations of the vertical velocity. The result $k_h \phi_w(k_h)$ normalized by w_*^2 and z_i is shown for $z/z_i = 0.64$ in Figure 10. In the inertial subrange a slope of $-2/3$ is to be expected for $k_h \phi_w(k_h)$ in the logarithmic scales. The maximum resolved wavenumber is $k_h z_i = 50$ in the simulation. The computed spectrum shows that the simulation exhibits the inertial subrange and that energy peaks at about the same wavenumber as in the experiment.

From the comparison we conclude that MESOSCOP can be sucessfully applied to simulate the CBL. No such simulations have been reported in the literature for the experiment DW85 before. The simulation should be extended to larger grids and to longer periods of time to further support the findings. The present results suggest that a second order subgrid scale model is required unless the grid scales are small enough to resolve the inertial subrange. Then a first order model gives sufficient accuracy.

3.5 Simulation of an Observed Convective Cloud

Data obtained on July 19, 1981 during the CCOPE (Cooperative Convective Precipitation Experiment) experiment in Montana are chosen as a test case for the physical treatment of clouds in MESOSCOP. The cloud observed on this day was a small, short-lived thunderstorm, well documented by radar and aircraft measurements (DYE et al., 1986). This case is of special interest because it is a mixed phase cloud, where both liquid and ice phase processes can be studied. A rather isolated updraft has been observed, which makes it easy to identify structures for validation. The case has been subject of a cloud modelling workshop (WMO, 1986).

The observations show that the cloud grows out of a field of cumulus mediocris with tops at 6.5 km MSL. Between 1621 and 1632 MDT (Mountain daylight time) the cloud exhibits a rapid growth phase and the top of the cloud shoots up to 11.5 km. The cloud diameter is approximately 6 km at all levels, the cloud base is observed at 4 km MSL. The cloud's life cycle is typical for a single cell: an active growth phase followed by a dissipating phase accompanied by (weak) downdrafts and precipitation. Measurements revealed cloud droplets with diameters of 8 to 10 μm in concentrations of 800 to 900 m^{-3} at the cloud base indicating that the coalescence process is inefficient in producing precipitation sized drops in the available growth time. The precipitation particles observed inside the cloud are graupels with maximum sizes of 7 mm. These particles are formed rapidly during the active growth phase of the cloud causing maximum radar reflectivities of up to 55 dBZ.

In the numerical model, the sounding of Miles City 1440 MDT is used to specify the profiles of the initial fields. Convection is triggered by imposing a constant entropy source of 0.1 $Wm^{-3}\,K^{-1}$ at the bottom of the model domain at 4 grid points. A constant 'mean' wind vector is subtracted from the wind field. This reduces numerical approximation errors. Moreover, it implies that the heat source moves with the mean wind and thus supports the formation of an organized updraft in a given air volume for a longer period. The model initiation time and the duration of heating at the bottom are matched to the observations by reference to the rapid growth phase of the cloud observed both in nature and in the model. Thus the model simulation starts at 1602, heating is switched on at 1604 and switched off 22 minutes later. This method of initialization is a crude approximation to the processes in nature but should be permitted for the purpose of validating parametrizations of cloud microphysics.

Periodic boundary conditions (type PERI) are used at lateral boundaries. The bottom and top boundaries are treated as closed (CLOS). Only precipitation falls out at the bottom. The integration is performed on a 16^3 km^3 domain with a spacing of 1 km horizontally and 0.8 km vertically. The time step is 20 s.

The present case has been simulated using both the Boussinesq variant and the variant with variable density for compressible air. The two results differ by up to 6 % for the velocity fields and somewhat more (typically 20 %) for cloud particle concentrations. Because of closed or periodic boundaries the system cannot expand and the mean pressure in the whole computational domain increases slightly (0.1 hPa) due to the entropy source. This causes a small temperature increase (0.07 K) and reduces the amount of condensed water. Sound waves do not play a noticeable role.

The dynamic and microphysical development of the model cloud is shown in Figure 14 at two selected times. Up to 1620 the cloud is a sheared cumulus mediocris consisting only of cloud droplets with a

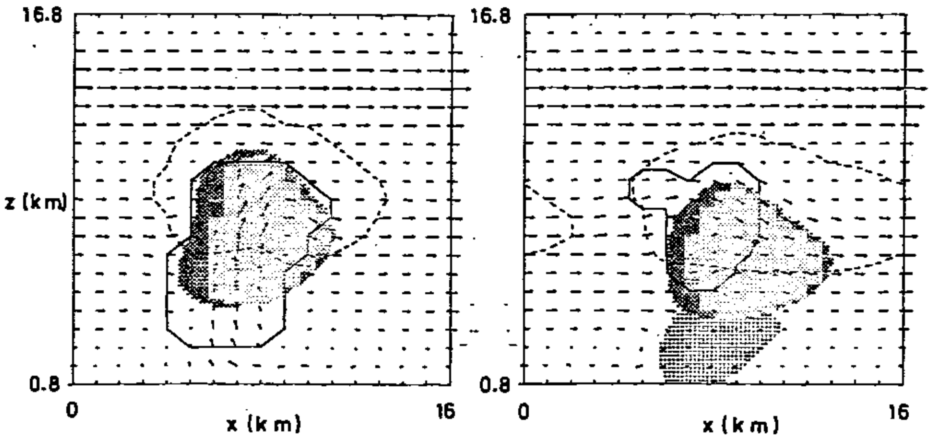

Figure 14 Vertical cross sections through the model cloud at 1632 (left) and 1644 MDT (right), showing the velocity field (maximum vector of 12.5 m/s at 1632 and 11.4 m/s at 1644 MDT), the outlines of the cloud droplet (solid line) and the cloud ice regions (dashed line), the regions of specific graupel (dark tone) and rain (light tone) content larger than 0.2 g/kg.

maximum mass specific concentration of about 1.2 g/kg. The cloud base is found at 2.4 km MSL which is 1.5 km lower than observed. This discrepancy may be explained by uncertainties in the sounding because we use the 1440 sounding of Miles City obtained earlier in time and at a different location. The rapid growth phase of the cloud between 1620 and 1632 has been found also in the model simulations. The vertical velocity in the updraft is about 12 m/s (with a maximum value of 20 m/s at one grid point) which is close to the observed values (10 to 15 m/s). At 1626 the first ice crystals are simulated in the upper cloud region and the maximum cloud water content (2.8 g/kg mean value) is reached at an altitude of 7 km MSL. At 1629 the first graupels appear in the mixed phase region. The graupels rapidly grow by riming thus consuming the available liquid water. The graupels fall downwards against the updraft which is now decreasing in magnitude because the entropy source has been switched off. Between 1635 and 1641 the falling graupel particles start melting when passing the freezing level at about 4 km height and initiate a rain shower reaching the ground at about 1640 which is in accordance with the observations.

The radar reflectivity factor Z is computed from the model results according to

$$Z = 10 \log \left[\frac{1}{Z_*} \sum_{k=3}^{7} Z_k \right] \quad \text{with} \quad Z_k = \int_0^\infty D^6 f_k(D)\, dD, \tag{46}$$

where D stands for the particle diameter (in mm), $f_k(D)$ for the size distribution of particle class k (in $m^{-3}\,mm^{-1}$; cf. HÖLLER, 1986), and where $Z_* = 1\ mm^6\,m^{-3}$ denotes a normalizing factor. In Figure 15 computed and measured reflectivities are shown for one selected time (1632 MDT). These results and those for other times (not shown) reveal that the model radar echo develops somewhat slower than the observed reflectivity. At 1620 there is no radar echo in the model, at 1626 the − 5 dBZ contour is reached at 6.4 km MSL while the observations show 0 dBZ at 1620 and up to 20 dBZ in 7 km height at 1626 MDT. There are several possible reasons for these differences: the matching of the time scale

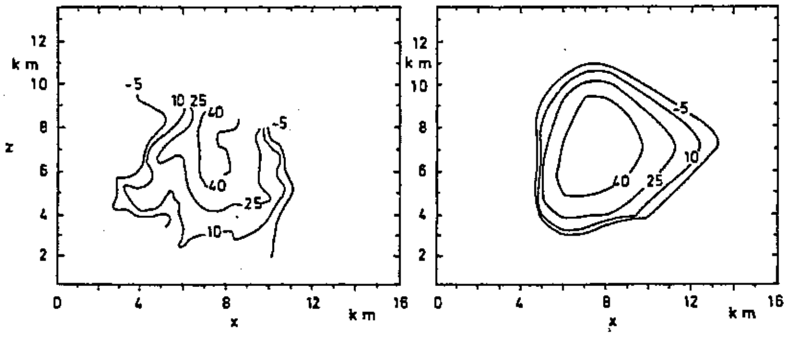

Figure 15
Vertical cross sections of observed (left, after DYE et al. 1986) and calculated (right) radar reflectivity factors in dBZ for 1632 MDT.

for comparison of model results and observations may be inadequate or the microphysical parametrization may underestimate the initial formation rate of precipitation. Also, the simulation exhibits a single updraft in which precipitation particles are formed while observations indicate a pre-existing cloud turret (NW-turret, see DYE et al. 1986) which may have produced ice particles subsequently incorporated into the second updraft (NE-turret). The maximum value and vertical extension of the reflectivities at 1632 coincide quite well in the model and in the observations. The 40 dBZ contour extends from about 5 km to 9.5 km height. The simulated horizontal extension of the precipitation is somewhat larger in the direction of the wind than observed. At 1641 precipitation reaches the ground but the precipitation shaft in the model is smaller and less intense (width 3 km, 30 dBZ) than observed (6 km observed width, 45 dBZ). This may be caused by the stronger horizontal displacement of precipitation in middle levels in the model cloud.

The main conclusions, which can be drawn from the preceeding comparisons, are: the formation of the precipitation particles via the ice phase is simulated correctly by the model; precipitation is mainly formed by riming; no warm rain process occurs, the snow processes are negligible; results for the speed and horizontal dimension of the updraft and the life cycle of the cloud do well agree with observations; an explosive growth phase is simulated, but the vertical dimension of the cloud is larger than observed; the maximum intensity of the radar echo is simulated reasonably well, but the computed horizontal extension is larger at middle levels and smaller near the ground than observed. In particular, this example shows that MESOSCOP provides the possibility of simulating variable density flows. The results of the Boussinesq case differ from the results with compressible air by approximately 20 % but do not exhibit significantly different structures.

4 Conclusions

The numerical model MESOSCOP has been introduced and validated for five cases as summarized in Table 4. All three versions of the model are used. The table indicates the binary choice features, which are tested in the various cases: variable density / Boussinesq density, non-hydrostasy/ hydrostasy, with/without Coriolis forces, with/without orography, with/without turbulence model and with/without cloud microphysics. The examples, for which analytical solutions are available, constitute a quantitative measure of the model's numerical accuracy. In the cases 'CBL' and 'cumulus' the positivity of the scalar advection scheme plays a significant role, because the nonlinear constitutive equations require non-zero values for concentrations and subgrid-scale kinetic energy. Radiating boundaries are selected from the variety specified in Section 2.4 for three cases; the BKD condition at the top is essential for the 'waves' case. The relative computational work caused by the pressure evaluation varies from a few percent for cases above flat terrain and with detailed parametrizations (direct pressure

■ **Table 4** Aspects of the model tested within the validation examples together with number of grid cells and time fraction for the pressure computation

aspect \ validation case	thermal	waves	front	CBL	cumulus
model version	A, B	B	B	C	A
variable density	no	no	no	no	yes
non-hydrostatic	yes	no	no	yes	yes
with Coriolis forces	no	no	yes	no	no
with orography	no	yes	yes	no	no
with turbulence model	yes	no	no	yes	yes
with cloud microphysics	no	no	no	no	yes
number of scalars	1	1	1	2	7
quant.test f. num.accuracy	yes	yes	yes	no	no
pos.adv.scheme significant	no	no	no	yes	yes
radiating bound.conditions	no	yes	yes	yes	no
number of grid cells	30 x 30 x 45	120 x 60	96 x 40	60 x 60 x 40	16 x 16 x 20
time fraction f. press.comput.	0.071	0.50	0.48	0.018	0.011

solution) to 50 % for cases with orography and simple physics (iterative pressure solution). The 'thermal' and 'CBL' cases demonstrate the ability to work with large three-dimensional grids that necessitate data segmentation on the computer used. The coded option of using variable grid spacings is not validated by the presented examples.

The possibility of applying the model for examinations of the validity of various approximations is indicated by comparing results with and without Boussinesq-approximation for the 'cumulus' case and by comparing the semi-geostrophic solution of DAVIES (1984) with numerical results for the 'front' case. Further results in this respect are discussed in SCHUMANN (1987b).

The simulation results of an inviscid rising thermal demonstrate the accuracy of the numerical method and identify the dependence of the results on the mean level of the scalar. For the diffusive thermal, the results agree excellently with the predictions of similarity theory. In contrast to some of the previous simulations, the present results are not controlled by numerical diffusion. In particular the integral variance of temperature exhibits the predicted trend although the Smolarkiewicz advection scheme does not necessarily conserve quadratic quantities.

The comparison with the hydrostatic Long-problem for gravity waves over mountains turns out to be successful, especially when taking into account the absence of any explicit damping mechanisms. The performance of the radiative top boundary condition (BKD) has been confirmed. The slight decrease of momentum flux with height in the non-linear case is not completly understood.

The results obtained for the orographic deformation of an idealized cold front agree very well with previous numerical results. The appearance of a hydraulic jump in accordance with theory does support the validity of the model. The presented results indicate the limitations of semi-geostrophic theories.

The large-eddy simulation of a convective boundary layer shows good agreement with laboratory experiments and allows one to determine turbulence statistics not computable from first or second order turbulence models. The results indicate that the grid spacings taken are small enough to resolve the eddies which carry most of the kinetic energy. The simulation is valid only as long as the lateral scales of the thermals are sufficiently small in comparison to the horizontal size of the computational domain. This is the case for the time period investigated so far.

Even though the simulation of the convective cloud was performed with rather coarse resolution, it reveales that the numerical technique and the microphysics parametrizations are well suited for this purpose. The results show in particular, that the observed precipitation is formed via the ice phase, while warm rain processes are negligible. However, the present simulation is strongly influenced by the rather artificial method used to initiate convection. Large scale influences or local disturbances from the boundary layer may be responsible for initiation in nature, but are not yet included in the model.

In general, the study demonstrates the wide range of scales (from centimetres to hundreds of kilometres) over which the model can be applied. It treats several physical processes including dry convection, gravity waves, turbulent motion, frontal motion and clouds including liquid and ice processes. Certainly, more physical processes like radiation or energy exchange at the ground will have to be added by proper parametrizations. The model can be applied for a large number of different boundary conditions, but extensions might become necessary (for example with respect to nesting; cf. CLARK and FARLEY, 1984).

The validation cases reported here represent a few successful steps forward in the never ending march of validating and improving a complex numerical model in the sense outlined by PIELKE (1984, p. 421). They contain convincing evidence that very different mesoscale processes can be treated with the described model framework. Extensions of the calculations presented are under way. They comprise comparisons with documented cases of strong airflow over mountains, the orographic deformation of cold fronts in three dimensions, and CBL calculations and studies of cumulus convection with increased resolution.

Appendix A: List of Symbols

a) for model formulation

t	time
$x, y, z; \xi, \chi, \eta$	Cartesian coordinates; transformed coordinates
div, $\mathrm{gr}\vec{\mathrm{a}}\mathrm{d}$	general divergence and gradient operators
$\rho, \overline{\rho}, \rho'$	total, reference and deviation density
$p, \overline{p}, p', p^i, p_*$	total, hydrostatic reference, deviation, air component partial and thermodynamic reference pressures
$\vec{v}, \rho\vec{v}, (\rho\vec{v})_G$	velocity, momentum, geostrophic momentum
$(\rho\vec{v})^\sim$	preliminary momentum without pressure gradient contribution
$\mathbf{F}, \mathbf{F}^t, \mathbf{F}^p$	total friction tensor, turbulent and precipitational parts
$\psi_k, q_k, \vec{v}_k^{\,term}$	k-th mass specific scalar, source term and terminal velocity vector
$\vec{f}_k, \vec{f}_k^{\,t}, \vec{f}_k^{\,p}$	total flux vector, turbulent and precipitational parts
k, K	index for and number of scalars
T, T_*, θ	absolute temperature and reference value, potential temperature
s, s_i, s_*, s_i^*	total and partial entropies, and respective reference values
R_m, c_p	gas constant and specific heat at constant pressure for cloud air
m^i, R_i, c_p^i	specific concentration, gas constant and specific heat at constant pressure for component i
A_p, A_k	coefficients in linearized equation of state
$\vec{g} = (0, 0, g)$	gravity of the earth (vector and Cartesian components)
$\vec{\Omega} = (0, \omega\cos\varphi, \omega\sin\varphi)$	rotation of the earth (vector and Cartesian components) as a function of latitude φ
z_s, z_t	orographic and model top heights

σ	terrain following coordinate, $(0 \leqslant \sigma \leqslant z_t)$
V, G^{ij}	Jacobian and metric coefficients of transformation
D, Δ, l, c_t	deformation tensor, grid resolution, mixing length and numerical constant in first order turbulence parametrization

b) for rising thermal simulations

$R, w_m, \theta'_m, h_w, h_\theta$	radius, maximum vertical velocity, maximum temperature surplus, vertical positions of velocity and temperature maxima
R_*, w_*, θ_*	reference scale for length, velocity and temperature
$E_{kin}, E_{pot}, E_\theta$	integral kinetic and potential energies, integral temperature variance
$t^* = t\, w_*/R_*$	non-dimensional time

c) for gravity wave simulations

m, N, U	vertical wave number, Brunt-Väisälä frequency, inflow velocity
δ	displacement height
θ_0	reference values for potential temperature
M	vertical flux of horizontal momentum
h, a	summit height and half width of bell-shaped mountain
$t^* = t\, U/a$	non-dimensional time

d) for simulations of frontal propagation

U_g, V_g	components of constant geostrophic wind
H_F, R, C	asymptotic front height, Rossby radius, gravity wave speed
H_B, L	summit height and width of sine-squared mountain profile
$f = 2\omega \sin\varphi,\ g' = g\, \Delta\theta/\theta_0$	Coriolis frequency and reduced gravity
$t^* = t\, U_g/L$	non-dimensional time

e) for convective boundary layer simulations

E	subgrid scale turbulent kinetic energy
β, Q_0, z_i	volumetric expansion coefficient, surface temperature flux, inversion height
w_*, T_*	convective vertical velocity and temperature scales (based on z_i)
w^*, T^*	convective vertical velocity and temperature scales (based on z_t)
k_h, ϕ	horizontal wavenumber, spectrum of horizontal variations

f) for cloud simulation

Z, Z_k, Z_*	total and particle class radar reflecivity, normalizing factor
$D, f_k(D)$	particle diameter, spectral size distribution

Appendix B: Time Integration Algorithm and Determination of Sources

In Section 2.2 the basic equations are given in time discretized form. Here the algorithmic sequence is described by which the equations are evaluated. Also, details of explicit or implicit treatment of source terms for scalar fields are explained.

Initial conditions for n = 0 prescribe ρ^n, $\vec{v}^n$, ψ_k^n and p^n at time t^n. These initial conditions have to be consistent with the equation of state and the boundary conditions. From the initial values we compute $p'^n = p^n - \bar{p}$ and a preliminary momentum $(\rho\vec{v})^{\sim} = \rho^n\vec{v}^n$. In general the preliminary initial momentum flux does not satisfy the continuity equation. Therefore, it is adjusted by the solution Δp of Poisson's equation for arbitrary positive Δt:

$$\operatorname{div}\vec{\operatorname{grad}}(\Delta p) = \frac{1}{\Delta t}\operatorname{div}(\rho\vec{v})^{\sim}, \tag{B1}$$

yielding $\operatorname{div}(\rho\vec{v})^n = 0$ with

$$(\rho\vec{v})^n = (\rho\vec{v})^{\sim} - \Delta t\,\vec{\operatorname{grad}}(\Delta p), \quad \vec{v}^n = \frac{(\rho\vec{v})^n}{\rho^n}. \tag{B2}$$

Starting from these initial conditions we compute in sequence for n = 0, 1, ...:

$$(\rho\psi_k)^{\sim} = \rho^n\psi_k^n - \Delta t\,[\operatorname{div}((\rho\vec{v})^n\psi_k^n) + \operatorname{div}(\vec{f}_k^n)] + \Delta t\,\rho^n q_k^{ex} \tag{B3}$$

$$\rho^{\sim} = \rho(p^n, (\rho\psi_k)^{\sim}) \quad \text{or} \quad \rho^{\sim} = \rho(p^n, \psi_k^{\sim}), \tag{B4}$$

$$\psi_k^{\sim} = \frac{(\rho\psi_k)^{\sim}}{\rho^{\sim}}, \tag{B5}$$

$$\psi_k^{n+1} = \psi_k^{\sim} + \Delta t\,q_k^{im}, \tag{B6}$$

$$\rho^{\sim} = \rho(p^n, \psi_k^{n+1}), \tag{B7}$$

$$A_p = (1 - f_B)\frac{\partial\rho(p^n, \psi_k^{n+1})}{\partial p}, \tag{B8}$$

$$\vec{b}^n = \operatorname{div}((\rho\vec{v})^n\vec{v}^n) + \operatorname{div}(F^n) + 2\vec{\Omega}\times[(\rho\vec{v})^n - (\rho\vec{v})_G], \tag{B9}$$

$$(\rho\vec{v})^{\sim} = (\rho\vec{v})^n - \Delta t\,[\gamma_0\,\vec{b}^n + \gamma_1\,\vec{b}^{n-1} + \vec{\operatorname{grad}}(p')^n + (\rho^{\sim} - \tilde{\rho})\,\vec{g}], \tag{B10}$$

$$r = \frac{1}{\Delta t}\operatorname{div}(\rho\vec{v})^{\sim} + \frac{1}{\Delta t^2}(1 - f_B)(\rho^{\sim} - \rho^n). \tag{B11}$$

Here $f_B = 1$ in the Boussinesq variant and $f_B = 0$ otherwise.
Now we invert the Helmholtz equation

$$\operatorname{div}\vec{\operatorname{grad}}(\Delta p) - \frac{A_p}{\Delta t^2}\Delta p = r \tag{B12}$$

to obtain the mass conserving pressure increments Δp. Finally, density, pressure and momentum are updated, and time is incremented to the next level:

$$\rho^{n+1} = f_B\,\rho^n + (1 - f_B)(\rho^{\sim} + A_p\,\Delta p), \tag{B13}$$

$$(p')^{n+1} = (p')^n + \Delta p, \tag{B14}$$

$$(\rho\vec{v})^{n+1} = (\rho\vec{v})^{\sim} - \Delta t\,\vec{\operatorname{grad}}(\Delta p), \vec{v}^{n+1} = \frac{(\rho\vec{v})^{n+1}}{\rho^{n+1}}, \tag{B15}$$

$$t^{n+1} = t^n + \Delta t. \tag{B16}$$

If the equation of state gives density as a function of mass specific concentrations, $\rho = \rho(p, \psi_k)$, then Equations (B4, B5) are solved iteratively or by using the approximation $\rho^{\sim} = \rho(p^n, (\rho\psi_k)^{\sim}/\rho^n)$.

Equation (B3) is actually split further according to SMOLARKIEWICZ (1984). Intermediate values in this splitting algorithm are computed with fixed density ρ^n.

The 'explicit' source q_k^{ex} in Equation (B3) comprises slow processes and sources which are explicit functions of time, $q_k^{ex} = q_k(t^n, p^n, \psi_k^n)$. The 'implicit' sources $q_k^{im} = q_k(p^n, \psi_k^{\sim})$ in Equation (B6) represent cloud phase fluxes or fast turbulent sources like dissipation of kinetic energy.

For cloud condensation (or evaporation) the amount of condensing water Δm per unit mass contributes to sources $q_2^{im} = -\Delta m/\Delta t$ for water vapour and $q_3^{im} = \Delta m/\Delta t$ of cloud water such that the concentration $m^1 = \psi_2$ approaches its saturation values m^{21} by an adiabatic and isobaric process. For large phase-changes per integration step it might be necessary to determine Δm iteratively according to this process. At present, we use the common explicit linearized approximation (LANGLOIS, 1973)

$$\Delta m = \frac{m^1 - m^{21}}{1 + \dfrac{m^{21}(l_{21})^2}{R_1 T^2 c_p}}, \qquad m^{21} = \frac{p^{21}(T)}{\rho R_1 T}, \tag{B17}$$

where l_{21} is the latent heat of vapourization, c_p the specific heat of the cloud-air, $p^{21}(T)$ the saturation pressure, and R_1 the gas constant of water vapour. All quantities are evaluated from p^n and $\psi_k^{\sim}$.

In order to avoid negative subgrid-scale kinetic energy E (per unit mass), the dissipation rate ϵ is treated by computing

$$E^{n+1} = E^{\sim} \exp\left\{-\frac{\epsilon}{E^{\sim}} \Delta t\right\} \tag{B18}$$

instead of Equation (B6).

References

ATKINSON, B. W., 1981: Meso-scale atmospheric circulations. Academic Press, London, 495 pp.

ATKINSON, B. W., 1984: The meso-scale atmosphere. Queen Mary College, Dept. of Geography and Earth Sciences, London, 32 pp.

BOUGEAULT, P., 1983: A non-reflective upper boundary condition for limited-height hydrostatic models. Mon. Wea. Rev. 111, 420–429.

CLARK, T. L., 1977: A small-scale dynamic model using a terrain-following coordinate transformation. J. Comput. Phys. 24, 186–214.

CLARK, T. L., 1979: Numerical simulations with a three-dimensional cloud model: lateral boundary condition experiments and multicellular severe storm simulations. J. Atmos. Sci. 36, 2191–2215.

CLARK, T. L. and R. D. FARLEY, 1984: Severe downslope windstorm calculations in two and three spatial dimensions using anelastic interactive gridnesting: a possible mechanism for gustiness. J. Atmos. Sci. 41, 329–350.

CLARK, T. L. and W. R. PELTIER, 1977: On the evolution and stability of finite-amplitude mountain waves. J. Atmos. Sci. 34, 1715–1730.

DALEY, R. and P. MERILEES, 1971: A spectral model of bubble convection. J. Atmos. Sci. 28, 933–943.

DAVIES, H. C., 1984: On the orographic retardation of a cold front. Beitr. Phys. Atmosph. 57, 409–418.

DEARDORFF, J. W. and G. E. WILLIS, 1985: Further results from a laboratory model of the convective boundary layer. Bound. Layer Meteor. 32, 205–236.

DeGROOT, S. R. and P. MAZUR, 1969: Grundlagen der Thermodynamik irreversibler Prozesse. B. I. Hochschultaschenbücher 162 / 162a, Hochschultaschenbücher-V., Mannheim, 217 pp.

DURRAN, D. R. and J. B. KLEMP, 1983: A compressible model for the simulation of moist mountain waves. Mon. Wea. Rev. 111, 2341–2361.

DYE, J. E., J. J. JONES, W. P. WINN, T. A. CERNI, B. GARDINER, D. LAMB, R. L. PITTER, J. HALLETT and C. P. R. SAUNDERS, 1986: Early electrification and precipitation development in a small, isolated Montana cumulonimbus. J. Geophys. Res. 91, 1231–1247.

FINGER, J. E. and H. SCHMIDT, 1986: On the efficiency of different higher order turbulence models simulating the convective boundary layer. Beitr. Phys. Atmosph. 59, 505–517.

FOX, G. D., 1972: Numerical solution of three-dimensional, shape-preserving convective elements. J. Atmos. Sci. 29, 322–341.

FRENZEN, G., D. HEIMANN and M. WAMSER, 1987: Dokumention des Regionalen Klimamodells (RKM) auf der Basis von FITNAH. DFVLR-Mitteilung 87–07.

GROSS, G., 1985: An explanation of the 'Maloja-Serpent' by numerical simulation. Beitr. Phys. Atmosph. 58, 441–457.

HADERLEIN, K., 1986: Numerische Modellrechnungen zum Verlagerungsverhalten orographisch modifizierter Kaltfronten. Diplom-Thesis, Meteor. Inst., Ludwig-Maximilians Universität München.

HARLOW, F. H. and A. A. AMSDEN, 1971: A numerical fluid dynamics method for all flow speeds. J. Comput. Phys. 8, 197–213.

HAUF, T. and H. HÖLLER, 1987: Entropy and potential temperature. J. Atmos. Sci., in press.

HAUF, T. and J. WEIDNER, 1986: The calculation of the entropy distribution along cloud traverses using aircraft measurements. Meteorol. Rdsch. 39, 33–36.

HÖLLER, H., 1986: Parametrization of cloud-microphysical processes in a three-dimensional convective mesoscale model. DFVLR-Forschungsbericht 86-02.

HOINKA, K.-P., 1985: A comparison of numerical simulations of hydrostatic flow over mountains with observations. Mon. Wea. Rev. 113, 719–735.

HOUGHTON, D. D. and A. KASAHARA, 1968: Nonlinear shallow fluid flow over an isolated ridge. Comm. Pure Appl. Math. 21, 1–23.

JANK, T., 1984: Zur Lösung der LONG-Gleichung bei hydrostatischer Gebirgsüberströmung. DFVLR-Mitteilung 84-02.

KLEMP, J. B. and D. R. DURRAN, 1983: An upper boundary condition permitting internal gravity wave radiation in numerical mesoscale models. Mon. Wea. Rev. 111, 430–444.

KLEMP, J. B. and D. K. LILLY, 1978: Numerical simulation of hydrostatic mountain waves. J. Atmos. Sci. 35, 78–107.

LANGLOIS, W. E., 1973: A rapidly convergent procedure for computing large-scale condensation in a dynamical weather model. Tellus 25, 86–87.

LILLY, D. K., 1962: On the numerical simulation of buoyant convection. Tellus 14, 148–172.

LILLY, D. K., 1964: Numerical solutions for the shape-preserving two-dimensional thermal convection element. J. Atmos. Sci. 21, 83–98.

LILLY, D. K. and J. B. KLEMP, 1979: The effects of terrain shape on nonlinear hydrostatic mountain waves. J. Fluid Mech. 95, 241–261.

LIN, Y. L., R. D. FARLEY and H. D. ORVILLE, 1983: Bulk parametrization of the snow field in a cloud model. J. Clim. Appl. Meteor. 22, 1065–1092.

KOENIG, L. R., 1971: Numerical modeling of ice deposition. J. Atmos. Sci. 28, 226–237.

MAHRER, Y. and R. A. PIELKE, 1977: A numerical study of the airflow over irregular terrain. Beitr. Phys. Atmosph. 50, 98–113.

MAHRER, Y. and R. A. PIELKE, 1978: A test of an upstream spline interpolation technique for the advective terms in a numerical mesoscale model. Mon. Wea. Rev. 106, 818–830.

MELLOR, G. L. and T. YAMADA, 1982: Development of a turbulence closure model for geophysical fluid problems. Rev. Geophys. Space Phys. 20, 851–875.

NICKERSON, E. C., E. RICHARDS, R. ROSSET and D. R. SMITH, 1986: The numerical simulation of clouds, rain and airflow over the Vosges and Black Forest mountains: a meso-β model with parametrized microphysics. Mon. Wea. Rev. 114, 398–414.

OGURA, Y., 1962: Convection of isolated masses of a buoyant fluid: a numerical calculation. J. Atmos. Sci. 19, 492–502.

OGURA, Y. and N. A. PHILLIPS, 1962: Scale analysis of deep and shallow convection in the atmosphere. J. Atmos. Sci. 19, 173–179.

PIELKE, R. A., 1984: Mesoscale meteorological modeling. Academic press, Orlando, USA, 612 pp.

SCHUMANN, U., 1984: Conservation properties of finite difference Euler equations. ZAMM 65, T243–T245.

SCHUMANN, U., 1987a: The countergradient heat flux in turbulent stratified flows. Nucl. Engrg. Des. 100, 255–262.

SCHUMANN, U., 1987b: Influence of mesoscale orography on idealized cold fronts, J. Atmos. Sci., in press.

SCHUMANN, U. and R. A. SWEET, 1987: Fast Fourier transforms for direct solution of Poisson's equation with staggered boundary conditions. J. Comput. Phys., in press.

SCHUMANN, U. and R. FRIEDRICH (Eds.), 1986: Direct and large eddy simulation of turbulence. Notes on Numer. Fluid Mech. Vol. 15, Vieweg, Braunschweig.

SCHUMANN, U. and H. VOLKERT, 1984: Three-dimensional mass- and momentum-consistent Helmholtz-equation in terrain-following coordinates. In: W. Hackbusch (Ed.), Notes on Numer. Fluid Mech. Vol. 10, Vieweg, Braunschweig, 109–131.

SCORER, R. S., 1958: Natural aerodynamics. London, Pergamon Press, 322 pp.

SMAGORINSKI, J., 1963: General circulation experiments with primitive equations. Part I: the basic experiment. Mon. Wea. Rev. 91, 99–164.

SMITH, R. B., 1979: The influence of mountains on the atmosphere. Adv. Geophys. 21, 87–230.

SMITH, R. B., 1986: Mesoscale mountain meteorology. In: GARP Pub. Ser. 27, Scientific results of ALPEX, Vol. II, ICSU/WMO (WMO/TD No. 108), Geneva, 407–424.

SMOLARKIEWICZ, P. K., 1984: A fully multidimensional positive definite advection transport algorithm with small implicit diffusion. J. Comput. Phys. 54, 325–362.

STEINACKER, R., 1981: Analysis of the temperature and wind field in the Alpine region. Geophys. Astrophys. Fluid Dyn. 17, 51–62.

TRIPOLI, G. J. and W. R. COTTON, 1981: The use of ice-liquid water potential temperature as a thermodynamic variable in deep atmospheric models. Mon. Wea. Rev. 109, 1094–1102.

TRIPOLI, G. J. and W. R. COTTON, 1982: The Colorado State University three-dimensional cloud / mesoscale model-1982; part I: general theoretical framework and sensitivity experiments. J. Rech. Atmos. 32, 185–219.

VOLKERT, H. and U. SCHUMANN, 1985: Development of an atmospheric mesoscale model on a Cray – Experiences with vectorization and input/output. In: W. Schönauer (Ed.): Notes on Numer. Fluid Mech. Vol. 12, Vieweg, Braunschweig, 221–232.

VOLKERT, H. and U. SCHUMANN, 1986: Development of an atmospheric mesoscale model – setting up the version in terrain following coordinates. In: D. Rues and W. Kordulla (Eds.): Notes on Numer. Fluid Mech. Vol. 13, Vieweg, Braunschweig, 375–382.

WILHELMSON, R. and J. ERICKSEN, 1977: Direct solutions for Poisson's equation in three dimensions. J. Comput. Phys. 25, 319–331.

WISNER, C., H. D. ORVILLE and C. MYERS, 1972: A numerical model of a hail bearing cloud. J. Atmos. Sci. 29, 1160–1181.

WIPPERMANN, F., 1981: The applicability of several approximations in meso-scale modelling – a linear approach. Beitr. Phys. Atmosph. 54, 298–308.

WMO, 1986: Report of the international cloud modelling workshop/conference at Irsee, FRG. WMP Rept. No. 8, WMO/TD No. 139, Geneva.

WYNGAARD, J. C., 1985: Structure of the planetary boundary layer and implications for its modeling. J. Clim. Appl. Met. 24, 1131–1142.